What will Diamond II do for you?

PHAS0052: Group 10

Jialun Liu, Aarron Westerby, Yishen Duan, Chun Yin Leong, Liam Shanahan, Rifat Mahmmod, David Trieu, Meiyin Shuai

Supervisor: Dr. Roger Johnson

Project Start: Wednesday 15th January 2020
Project Conclusion: Friday 27th March 2020

University College London
Gower Street, London, WC1E 6BT

Executive Summary

This report will investigate the planned upgrade to the 'Diamond' light source, a 3rd generation synchrotron near Didcot Oxfordshire. It aims to evaluate the impact that the upgrade, named Diamond II, will have on the future scientific community.

A synchrotron is a large ring that accelerates electrons to high energies in order to emit electromagnetic radiation at specific locations along the ring. This radiation is captured within 'branch-line' facilities that protrude tangentially from the ring and are used for various experiments.

In this investigation we primarily focused on the I13-1 branch-line's coherent diffraction imaging (CDI) experiment, which aims to use coherent x-rays to accurately image Nano-scale structures. Coherence is an important factor in this experiment as it is the dominant determinant for resolution of the reconstructed image. A computational model was created to mimic the parameters, particularly coherence, of Diamond before and after the upgrade, allowing us to evaluate its potential success.

Further research was also undertaken to study how current experiments at the facility will benefit from the upgrade, and to research potential new experiments that are would become possible with the higher energy levels provided by Diamond II.

A field trip was organised to the current Diamond facility. The trip was used for the retrieval of data on the specifications of the upgrade as well as to gain key insight into current Diamond's machine parameters, this provided the team with a deeper understanding of the specific devices that are being replaced to upgrade the facility and how individual research teams will benefit from the Diamond II project.

The findings from our computational model demonstrated that both Diamond I and II have extremely near coherent beams, due to their low emittance (spread in position-momentum space). It was found that image resolution of the CDI method would hence be unchanged by the Diamond II upgrade. However, when considering the drastic increase in the value of brilliance in Diamond II, more data would be collected, making experiments conducted after the upgrade able to construct the images faster. This will increase the scientific output of the facility.

Furthermore, from investigating other facilities it was found that for Diamond, the UK's only 3rd generation synchrotron, to remain competitive and attract future investment to support its current research output (and fund further research) the facility would need to upgrade to compete with facilities such as ESRF-EBS and MAX IV. Therefore, when considering these factors, it is critical that the facility be upgraded to advance the ever pursuit of scientific knowledge and lay the foundations so that future scientists can achieve even more ground breaking work at this facility.

Contents

1 – Allocation of Work

Rifat Mahammod : Conducted literature review on past and present synchrotron upgrade programmes. Contributed to report writing of the background and conclusion section, including formatting the entire document. Main editor of the final poster. Attended Diamond Light Source trip.

David Trieu: Served as communications officer. Researched and wrote about the engineering details of the Diamond II upgrade. Outlined and contributed relevant parts of research done to conclusion.

Meiyin Shuai: Wrote the background and method of the coding section(mainly the algorithm of coherent diffraction imaging) and also coded the Hybrid-input algorithm. Researched and wrote the physical characteristics of the stored electron and X-ray beams, i.e. the emittance. Conducted the appendix.

Chun Yin Leong: Made advanced room bookings for all 5 meetings. Authored the theories on the productions of electrons & x-rays (13 pages condensed to 3 pages). Proposed a poster design, and contributed to poster editing. Summarized the theory for presentation. Co-edited the Formal Report. Helped with the correction of errata.

Yishen Duan: Researched on the scientific advancement the upgrade brought. Wrote sections in the background and conclusion. Coded the frame of the phase retrieval part of the computer simulation and the code to enable arbitrary Proposed a poster design.

Aarron Westerby: Aided the research and coding in the initial phase of the coding assignment and finalised the theory of CDI and method section in the report. Wrote the executive summary and finalised the conclusion and coded the wave simulation example.

Jialun Liu: Researched and coded the 2-dimensional phase retrieval algorithms (Error Reduction and Gerchberg–Saxton algorithms) for coherent diffraction imaging. Finalised the results and analysis. Contributed in the contents of the poster and edition of the report.

Liam Shanahan: Primary editor of the formal report, responsible for the structure and coherence of the final report. Worked in partnership with the poster team for the design of the poster.

2 – Background

This introductory section will first consider how a synchrotron works, focusing on the production and acceleration of electrons and the extraction of X-rays. Next, the potential for synchrotron upgrades, as well as the specifics of the Diamond II upgrade will be discussed. The experiments currently being conducted at the Diamond facility will be examined, including their potential for improvement after the upgrade. After considering how other synchrotron facilities around the world have benefited from similar upgrades, focus will be placed on a single experimental method currently in use at Diamond, 'Coherent Diffraction Imaging'. Further in the report, 'Coherent Diffraction Imaging' will be computationally modeled in order to quantitatively portray the benefits of the upgrade.

2.1 – How does a synchrotron work?

'Synchrotron' is the name given to a facility that accelerates electrons around a loop of fixed radius in order to produce high energy electromagnetic radiation. The Diamond facility predominantly produces radiation in the X-ray range of the spectrum.

A synchrotron has six major components: an electron source, booster ring, storage ring, radio-frequency (RF) supply, insertion devices and beamlines. Electrons produced at the source are accelerated through a linear accelerator ('Linac'), a smaller 'booster' ring and a larger 'storage' ring. Energy losses are compensated for in the storage ring using RF 'cavities'. Insertion devices then cause the fast-moving electrons to produce high intensity x-rays, which are collected for experimental use in the 'beam-lines'.
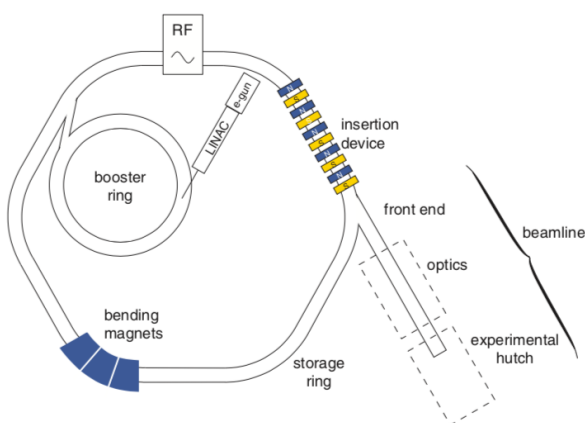

Figure 1: A schematic representation of the vital components of a synchrotron source [1].

2.1.1 – The Electron Source

Electrons are usually generated by thermionic emission via an "electron gun". Thermionic emission involves the liberation of electrons from an electrode by virtue of its temperature. When electricity flows through a tungsten-oxide cathode heated to around 1000°C, some electrons absorb enough energy to leave the surface of the cathode, causing them to "boil" off.
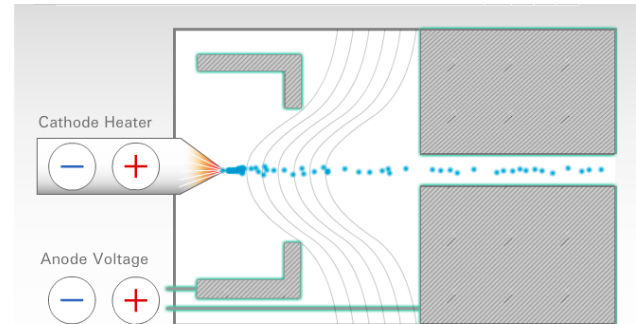

Figure 2: An electron gun releasing electrons by thermionic emission. When enough energy is applied, electrons escape from the surface [2].

These liberated electrons may then be accelerated by earthed anodes. As electrons are leaving the cathode, a nearby screen is given a strong positive charge (125 times per second) [3]. This pushes electrons towards the Linac, and away from the cathode. Simultaneously, a high voltage of around 200 kV in the cathode also repels the electrons and contributes to their acceleration towards the Linac. Electrons in this phase of the acceleration obtain energies of up to 90 keV.

The Linac utilises the Lorentz force to accelerate electrons to higher speeds. Since a single electromagnet would require extremely high voltages to supply an adequate force onto the electrons, a series of smaller magnets are used instead. As depicted in Fig. 3, the Linac consists of an array of radio-frequency (RF) cavities with fields oscillating at 2856 MHz. As the electrons are accelerated, they pass through a series of chambers that contain alternating electric fields. Consequently, the electrons always see a positive field ahead of them, towards which they accelerate. Each tube becomes longer for the electrons to pass through, because the accelerating electrons take a shorter time to cover a unit distance.
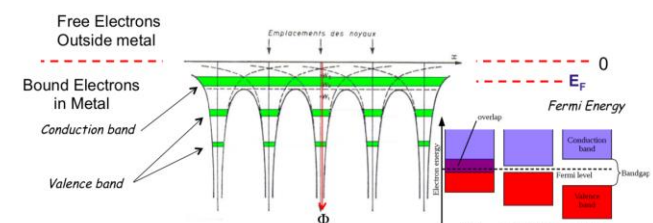

Figure 3: A schematic of the energy of bound electrons in a metal [4].

The electrons are accelerated to 100 MeV in this phase. At this energy, they travel very close to the speed of light. Pulses of electrons are produced by the Linac ranging from

2 ns to 140 ns which are then injected into the storage ring. During the normal mode of operations, long pulses generate a 420-ns pulse train per second. After several minutes, enough electrons have been generated into the storage ring allowing the synchrotron to function for a long period of time without the use of the Linac. Electrons are refilled regularly as collisions with residual gas particles results in electron loss in the storage ring. The Linac is able to produce short pulses of electrons called "bunches", which allows a constant flow of electrons in the storage ring.

Figure 5: A simplified structure of the Linac. Electrons liberated from an electron gun travel to the right through a series of chambers of increasing lengths [2].

2.1.2 – Booster Ring

At Diamond, electrons with energies of 0.1 GeV are injected from the Linac into the booster ring [5]. The ring has an 'athletics track' shape. In the straight sections, electrons are accelerated using a radio-frequency voltage source. Electrons are guided around curved segments using 36 dipole bending magnets. Electrons are periodically injected into the storage ring to maintain the specified storage ring current. This is performed when the storage ring current decreases to about $1-1/e \approx 70\%$ of the initial current [1].

2.1.3 – Storage Ring

The storage ring contains the electrons and maintains them on a closed path using magnets, collectively called the "magnet lattice" of the ring. At Diamond, there are approximately 900 electron bunches in the storage ring at any one time, each travelling around the ring 10^5 times per second. The magnets are classified into three common types: dipole (or bending), quadrupole, and sextupole magnets.

a) Dipoles

Dipoles are used to bend the path of the electrons. An electric field is applied, causing moving charges to change direction via the Lorentz force. Since the Lorentz force acts in a direction perpendicular to the direction of the electrons' velocity, an appropriate alignment and magnetic field strength will cause electrons to maintain the synchrotron radius in circular motion.
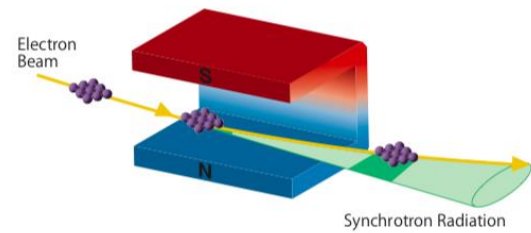

Figure 6: Electron bunches being bent by a dipole magnet.

b) Quadrupoles

Quadrupoles produce a linear field variation across the electron beam. They are used to focus the electron beam and compensate for the Coulomb repulsion between the electrons. The resulting field is zero at the magnetic centre, meaning the on-axis component of the beam is not bent, whilst off-axis components are guided to the centre.

c) Sextupoles

Sextupoles correct for chromatic aberrations (a defocusing of the electron beam due to dispersion) arising from the quadrupoles. The field in a quadrupole varies as the square of the displacement [6], meaning that off-momentum particles are incorrectly focused. Sextupoles modify transverse oscillation frequencies, correcting this effect.
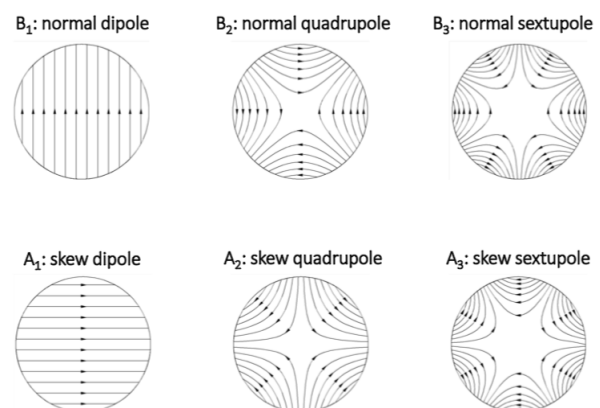
Figure 7: Magnetic field lines of a dipole, quadrupole, and sextupole, with their skew counterparts [7].

The interior of ring is kept at near vacuum conditions to minimise energy loss due to electrons scattering off of air molecules. Electrons in the storage ring complete a circuit with an energy of approximately 3 GeV.

2.1.4 – X-Rays

Electromagnetic radiation is emitted when a relativistic electron is forced to change direction. This phenomenon is exploited to produce x-rays using 'undulators', and 'wigglers' [8], contained within 'insertion devices' along the storage ring.

For a relativistic electron, any acceleration (in this case radial) results in a re-arrangement of the field around the charge, which causes a perturbation to radiate outwards at the speed of light. This results in the production of high intensity photons, known as synchrotron radiation. Synchrotron radiation is particularly useful for experimental use because it has a high flux, high brilliance, and is both linearly and circularly polarised (these features will be examined in further detail throughout this report). Although an ordinary bending magnet would stimulate synchrotron radiation, wigglers and undulators exaggerate this effect by causing electrons to oscillate.

Wigglers

Wigglers can be thought of as a sequence of bending magnets and are therefore more powerful than a single bending magnet. The angular deflection of the particle beam is much greater than the natural opening angle of the radiation. The radiation spectrum appears to be 2N dipole sources, where N is the number of oscillations in the wiggler. The power radiated by a wiggler is increased when the gap between the upper and lower sets of the wiggler's magnets are reduced. In fact, the radiation emitted by successive dipoles do not overlap. Thus, wigglers generate high-power x-ray beams with broad spectral ranges.

Undulators

The angular deflection is comparable to the divergence of radiation. The radiation from each pole overlaps and interferes with one another. Due to this feature only certain wavelengths interfere constructively, resulting in the undulator's spectrum comprising of a fundamental frequency with additional higher harmonic frequencies.

2.1.5 – Beamlines

All experimental applications of synchrotron radiation take place in facilities around the circumference of the storage ring known as 'beamlines'. The beamlines extend tangentially from the storage ring, along the axes of the insertion devices. Diamond I can host up to 33 beamlines. Each beamline is subdivided into four main sections:

- The Front end
  a) Extracts the x-ray beam by defining the angular acceptance of the radiation through an aperture
  b) Controls and monitors the beam's position
  c) Optionally filters Bremsstrahlung radiation and the low-energy beam of the synchrotron radiation, which may damage optical components.
- Optics hutch, where specific wavelengths are picked (monochromated) and focused.
- Experimental hutch, where the experimental laboratory is placed.
- Control cabin, where the scientific team monitors and analyses the experimental data.

As a safety precaution for beamlines that operate with high-energy x-rays, the hutches are shielded with concrete walls to protect researchers from dangerous radiation. These dangerous by-products can be produced in the storage ring when relativistic electrons collide with stray gas particles.
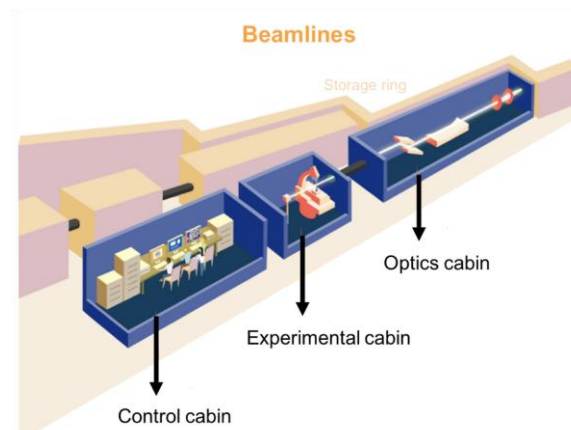

Figure 11: Structure of a beamline, tangentially extending out from the storage ring [9][10]

2.2 – Potential Improvement Factors

Several parameters of Synchrotron radiation and detection determine how useful it is as an experimental tool. The Diamond II upgrade will benefit primarily from improvements to the beam's resolution and emittance. These concepts are introduced in this section, and their usefulness quantified at a later stage of this report.

2.2.1 - Resolution

The three major types of resolution in an X-ray synchrotron are spatial, dynamic and energy resolutions. Spatial resolution refers to the precision of a measurement with respect to space, denoting the accuracy within a particular range of positions. The dynamic resolution is analogous to how more details can be found on a picture taken by a high-quality camera; dynamic resolution essentially allows data collection at a higher rate. This means the evolution of the sample can be better retrieved. Energy resolution determines the sensitivity of a detector with regards to radiation detection. Cameras with higher energy resolution can produce brighter images.

Currently, the quality of the equipment and resolutions in Diamond falls within the standard of '3rd generation'. Multiple beamlines in Diamond I require machinery upgrades in order to obtain measurements with higher precisions. This is highlighted by the fact that the current level of spatial resolution cannot support the determination of submicron structures, and the low rates of data collection limit understanding of processes happening within microseconds. Improving resolution has become a major justification towards Diamond's upgrade.

2.2.2 - Emittance

Emittance is a key property of a charged particle beam in accelerator physics. It measures the average spread of a particle's coordinates in position and momentum phase space and is described by Hamiltonian mechanics.

In the 3-dimensional real world (i.e. excluding time evolution of the system as the 'fourth' dimension), the emittance in the position and momentum phase space has 6 axes (px, py, pz, x, y, z) and thus forms a 6-dimensional phase space. The emittance can be measured in all three spatial Cartesian coordinates (x, y, z). The value of emittance, expressed as the dimension parallel to the direction of motion of particles (in the $z - pz$ plane), is known as the longitudinal emittance. The emittance in the dimension perpendicular to the direction of motion of particles ($x - px$ plane and $y - py$ plane) is known as the transverse emittance. The transverse emittance can be broken down into two components, the horizontal phase plane ($x - px$ plane) and the vertical phase plane ($y - py$ plane).

Transverse Emittance

Consider the intensity distribution function of the beam $f(x, y, z, px, py, pz)$, with x, y, z, px, py, pz as independent variables of the 6-dimensional phase space. By definition, the parameters of the phase space are independent from each other and so the intensity distribution function of the beam can be considered as the product of 3 independent intensity distribution functions in the $x - px$ plane, $y - py$ plane and $z - pz$ plane, respectively. We have assumed that the intensity distribution in each plane is a Bi-Gaussian distribution:

$$f(x, p_x) = \frac{1}{2\pi\sigma_x\sigma_{p_x}} \exp\left(-\frac{x^2}{2\sigma_x}\right) exp\left(-\frac{p_x{}^2}{2\sigma_{p_x}}\right)$$

Where $f(x, p_x)$ describes the Gaussian distribution and σ variables denote the half-widths of the Gaussian distribution. Note that the integral of the Gaussian distribution function across all of space results is the following:

$$\iint\limits_{allspace} f(x, p_x) = \frac{1}{2\pi\sigma_x\sigma_{p_x}} \int\limits_{-\infty}^{\infty} \exp\left(-\frac{x^2}{2\sigma_x}\right)dx \cdot \int\limits_{-\infty}^{\infty} \exp\left(-\frac{p_x{}^2}{2\sigma_{p_x}}\right)dp_x = 1$$

The source size/spatial extension can be characterized by the standard deviation of the intensity distribution in x, y planes. The angular divergence/distribution of the beam flux can be characterized as the standard deviation of the intensity around a nominal direction, (x', y'), with respect to the horizontal and vertical phase planes respectively.

Using these results, the transverse emittance in the horizontal and vertical phase plane ($\varepsilon x, \varepsilon y$) can be defined:

$$\varepsilon_x = \sigma_x\sigma_x$$

$$\varepsilon_y = \sigma_y\sigma_y$$

Where σ represents the standard deviation of each respective distribution, and the following relation has been inferred:

$$Emittance = Source\ Size \cdot Angular\ Divergence$$

Benefits of Low Emittance

As will be examined further in this report, the emittance of a synchrotron beam has a key influence over its experimental practicality. In particular, a lower emittance has the following properties.

1. Greater the likelihood to result in higher luminosity.
2. More concentrated x-ray beam, resulting in higher brightness.
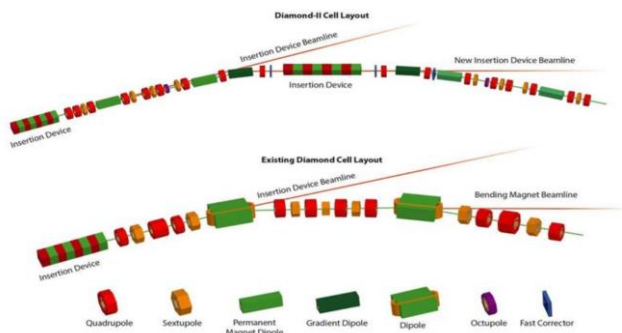3. Lower spread in phase space, leads to a more coherent beam of radiation

This introduces the inference that a beam of greater brightness, luminosity and coherence may be of greater experimental use. This assumption is the basis of the investigational segment of this report.
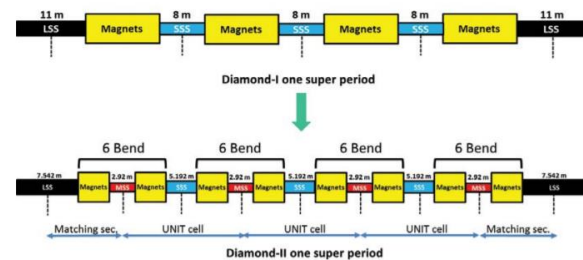
2.3 – Diamond Upgrade Details

Diamond II will be a substantial upgrade to the currently operating Diamond Light Source. It seeks to provide a world-class synchrotron facility that is competitive on an international scale both for academic researchers and industrial clients. The upgrade will encompass all operations and improve large portions of the current Diamond infrastructure. It will involve major machine and engineering upgrades with major improvements to beamlines, detectors, computing, software, optics and data storage. The design phase of the project is forecast to reach completion in 2022, with assembly starting shortly after, in 2023. At the time of writing, the entire upgrade is expected to finish in 2026 [11].

With global development of 4th generation synchrotron light sources, dramatic improvements in synchrotron light brightness and coherence (across increasing energy ranges) have been made, deriving from a reduction in horizontal electron emittance of one to two orders of magnitude. The proposed Diamond II lattice upgrade will consist of Double Triple Bend Achromats (DTBAs) (shown in Figure 13), which reduce the horizontal electron emittance by a factor of approximately 20, resulting in an increase in photon coherence and brightness. Another notable improvement is in the beam energy, which predicts an increase from 3.0 GeV to 3.5 GeV.

Figure 12. Photo of a section of the current Diamond storage ring taken on a visit during 10/03/2020 by our group. Green sections represent dipole magnets, red sections represent quadrupoles and orange sections represent sextupoles.

A replacement of Diamond I's bending magnets with insertion devices will improve the flux output, resulting in a greater beam energy (described by Figure 14). Although this alteration reduces coherence and marginally increases horizontal emittance (as detailed in Figure 15), it provides a significant net reduction in horizontal emittance (a factor of 20 compared to the current Diamond machine).

Figure 13. Schematic of current Diamond DBA (Double Bend Achromat) lattice (bottom) and new proposed design of Diamond II DTBA (Double Triple Bend Achromat) lattice (top). [12]

Figure 14. Brightness for a range of sources operating at Diamond (blue), Diamond II 3.0 GeV (green) and Diamond II 3.5 GeV (red). Brightness curves shown are respectively from left to right: I05 beamline, I21 beamline, future CPMU 15.6 mm period (installed on I11 beamline and VMXm), superconducting wiggler on I12 beamline.. [12]

Figure 15. Horizontal coherent fraction as function of energy for Diamond (blue), Diamond II 3.0 GeV (green), Diamond II 3.5 GeV (red). The coherent fraction is approximated as the ratio between brightness and calculated brightness in the limit of no energy spread and emittance [12]

A new novel development of a magnetic ('MBA') lattice devised by Diamond will maintain all the beamlines currently in operation without major structural changes, whilst also allowing for the addition of 5 new beam-lines. The lattice design consists of 24 cells with a long straight section after every four cells [13], as shown in Figure 16.

Figure 16. Schematic diagram of super-period structure of Diamond-II compared to Diamond currently. [12]

Each cell is roughly mirrored with respect to the 'Mid-Straight Section' (MSS) and is made up of 4 longitudinal gradient dipoles, 2 gradient dipoles, 16 quadrupoles (a further two pairs for each long straight section (LSS)), twelve sextupoles, two 'octupoles', and 'discrete correctors' facing into the long straights. Pairs of quadrupoles face the standard straight section (SSS), with triplets located in the LSS to produce zero dispersion. This will have the effect of focusing the beam further, as described in the initial section of this report. The longitudinal gradient dipoles reduce the emittance while the regular gradient dipoles contain an embedded quadrupole to lower spatial requirements.

There are multiple constraints involved in the optics design, the main ones being maintaining minimum straight section lengths, eliminating dispersion in LSS lengths, keeping a magnet-to-magnet spacing of 7.5 cm, and keeping dispersion below 2.5 cm in the MSS. As a consequence, the new gradient dipoles have a field of 0.7 T with gradient 30 T/m, whilst the quadrupoles have a gradient of 65 T/m.

Straight Section	Diamond	Diamond-II
long straight sections (LSS)	11.3 m	7.54 m
standard straight sections (SSS)	8.3 m	5.19 m
mid-straight sections (MSS)	3.4 m (DDBA)	2.92 m

Table. 1. Length of quadrupole to quadrupole straight sections for Diamond and Diamond II. [12]

Although this lattice design contributes primarily to emittance reduction, it can also increase the capacity of the storage ring, allowing for more beamlines. 5 new insertion devices will allow further beamlines by using various mid-straight sections and utilising free space on the experimental floor. Installation of the lattice and additional beamlines has been planned so as to minimise alterations to current beamlines, allowing on-going experiments and investigations to continue.

Parameter	Diamond (all IDs)	Diamond-II (all IDs)
Emittance [pm]	3100	125
Momentum compaction	1.56e-4	1.16e-04
Energy loss per turn [MeV]	1.52	1.53
Energy spread [%]	0.10	0.10
Horizontal damping partition	1.006	1.164
Vertical damping partition	1.000	1.000
Longitudinal damping partition	1.994	1.836
Horizontal damping time (ms)	7.36	7.37
Vertical damping time (ms)	7.40	8.58
Longitudinal damping time (ms)	3.71	4.67
Natural bunch length (ps)	10.99 @ 2.80 MV	10.78 @ 2.69 MV)

Table. 2. Main lattice parameters of Diamond and Diamond II. [12]

Converting all the current bending magnet beamlines to insertion device beamlines will produce more intense light, increasing the capacity for radiation exposure. As a result, Diamond II will construct additional shielding to keep the dose rate to $1\ mSv/y$.

Accompanying the storage ring upgrade will be various modifications and additions to existing beamlines, in order to best use the increased beam energy, brightness and coherence. One major example of this is the establishment of multilayer (ML) optic fabrication facilities, in-house, to directly control the manufacturing of mirrors and lenses used for focusing light. ML optics consisting of ML coated curved mirrors and Multilayer Laue Lenses are able to focus hard X-rays to sub-10nm, vastly improving the spatial resolution for many beamlines and experiments [14]. The increase in beam energy itself to 3.5 GeV contributes directly to the improvement in energy resolution since the greater photon flux allows a faster rate of data collection.

Diamond II is expected to capture vast amounts of data (Terabytes per second). This requires changes in data management and computation, necessary to sustain the increased output from all beam-lines. A new data centre will be created with an anticipated capacity of ~3 MW, vastly exceeding Diamond's currently operating 500 kW capacity. Computing and data management will be performed using in-house and external resources, with Cloud Computing and Machine Learning amongst new technologies to be implemented. New real-time 'in-memory' processing methods are being developed to process data as it comes from detectors, reducing strain on central servers. Greater processing power, coupled with high-speed detector equipment, will allow for improvements in dynamic time resolution of experimental measurements.

2.4 – Experimental Benefits of Diamond II

The improvements to Diamond allow for more advanced experimental techniques and precisions [15]. A particular experimental imaging technique, 'Coherent Diffraction Imaging', will be introduced in the next section, and examined quantitatively in the remainder of this report. This section, however, will summarise some of the numerous other experiments currently operating at Diamond, and describe how they will benefit from the Diamond II upgrade.

The upgrade will contribute to advancing both life and physical sciences. Not only will the upgrade improve the quality of machines, but also allow new technologies to be introduced to further fields of research.

2.4.1 - Advancing Life Sciences

Life Science studies are largely investigated through MX and Soft-Condensed Matter (SCM) beamlines in Diamond I. The upgrade will expand the experimental options and capacity as follows.

Integrated Structural Biology: Chromosome Structure

The complexity and density inside the chromosome of a metazoan makes it very difficult to probe, posing an issue for any structural imaging. Investigations made on such membrane proteins are very important, since 60% of drugs target them [16] (particularly G protein-coupled receptors (GPCRs)). Their study could provide information on the root cause of diseases such as cancer, obesity, depression and heart disease (conditions associated with mutations or 'mis-folding' of membrane proteins).

'In vivo' investigations by definition need to be carried out on live organisms, and the lack of dynamic resolution of the light source has posed great difficulties in keeping the organism alive until the end of data collection [17]. A higher flux and smaller emittance, enabled by Diamond II, will allow enough photon interaction with the organism for adequate data collection within a shorter time, reducing radiation damage.

Our understanding of the underlying structure of genomes has been limited by a lack of tools for 'in vivo' investigation and metazoan nucleus penetration. The higher flux and narrower beams provided by Diamond II will reduce this barrier to structure determination. Structural investigations' hierarchical phenomena such as epigenetics will be expanded with reduced radiation damage caused by

high-energy data collection, vacuum environments and next generation detectors.

Dynamic Studies

Diamond II allows the observation of micro-second macromolecule dynamics, which matches the timescale of the diffusion limit. This is a critical time resolution, at which most catalysis and bio-molecular processes occur at a slower rate [18]. This will in principle broaden the application of this method to most enzymes and support the increasing interest in optimising target-drug kinetics.

Biotechnology and Biological Systems

Diamond II enables physical characterisation and precision measurement of biomaterials at nano-scale precisions with:

- Brighter/harder X-ray beams to increase the penetration depth

- Improved spatial resolution in images

- New technologies involving 'Circular Dichroism' (CD) spectroscopy, 'Infrared' (IR) spectroscopy and 'X-ray Fluorescence Imaging'.

- Optimised beam characteristics (Coherence, Emittance, and Divergence).

2.4.2 - Advancing Physical Sciences

Energy

A broad range of research areas relevant to energy storage and generation will benefit from Diamond II, including solid oxide fuel cell technology, super-capacitors, bioenergy, solar-to-fuel, solid-state batteries, hydrogen storage and flow cells.

Current advancement in the study of soft-Resonant X-ray Inelastic Scattering (RIXS) has enabled comprehensive investigation of the electronic properties of oxygen and Sulphur ions in Li-rich and Na cathodes [19]. The process of electronic reconstruction from weak inelastic excitations is difficult using conventional X-ray absorption spectroscopy (XAS), but at Diamond II a multiplexed version of the RIXS spectrometer will allow data collection rates to be increased by a factor of 100. Monitoring the dynamics of light ions or atoms in an operational battery will be made possible at Diamond II through the development of novel instruments such as 'X-Ray Raman Scattering' (XRS) to perform spectroscopy studies of light elements.
Rechargeable batteries deteriorate in morphology over their lifetime. The increase in brilliance and phase contrast, due to the Diamond upgrade, will grant electrical engineers a better understanding of this process, with improved resolution in both space and time.

Chemistry

The improved X-ray brightness due to Diamond II, will enable further advancements of photon-in/photon-out techniques such as 'Valence to Core X-ray Emission Spectroscopy' (VtC-XES). The new research will overcome limitations Diamond I facility is that the currently facing. In particular, with VtCXES, it will be possible to distinguish neighbour ligands in the periodic table (such as carbon, nitrogen and oxygen).

Earth, Environment and Planetary Science

The increased coherence of Diamond-II will also contribute to the development of ptychography and Transmission X-ray Microscopy (TXM). By using phase contrast imaging, these techniques are able to locate organic carbon in the presence of 'porewater' ions. Consequently more advanced 3D mapping will lead to a better understanding of nano-scale minerals. In addition, faster raster scanning due to increase brightness, offers the possibility of real time data acquisition of chemical fractionation and transformation of organic carbon.

2.5 - Other Synchrotrons

The scientific advancements in fields such medicine and material sciences has resulted in an increase in demand for more advanced research equipment. In order to meet the needs of the global scientific community, continuous worldwide development of synchrotrons is taking place. Theoretical growth across various fields in biomedical sciences and solid-state physics has pressured engineers to design more sophisticated facilities, able to match and reproduce such theoretical progression. From engineering plans to improve X-ray production techniques to enhanced storage ring mechanisms, this section will explore world-wide synchrotron projects of the past and the future, and examine how such changes may improve research capacities.

2.5.1 - Past Synchrotron Projects

X-rays were first discovered in 1985 by W.C Rontgen as mysterious rays able to pass through the human body[20]. Since then, biomedical disciplines have advanced exponentially, resulting in remarkable discoveries, such as the intricacies of DNA structure. In addition to the immense expansion in the field of medicine, the use of X-rays have also played a crucial role in development of solid-state physics, with the first crystal diffraction pattern being obtained in 1912. The X-ray sources used in the past, X-ray tubes, were not ideal and presented limitations to experimental results. These devices emitted light in all directions. Lack of coherence became an imminent obstacle for research taking place in the field of spectroscopy and crystallography. Synchrotrons, first built in the 1960s, overcame the restrictions of X-ray tubes. Since then, a number of more sophisticated synchrotrons have been

developed around the world in order to improve brightness and coherence of x-rays.

ESRF Upgrade Programme

The European Synchrotron Radiation Facility (ESRF), first opened in 1994, was the first 3rd generation synchrotron source, capable of producing high brilliance and high-energy electron beams using modern insertion devices[21]. A large upgrade of the ESRF took place between 2008 and 2017 with the aim of meeting the demand for continuous technological advancement from the scientific community. The four main areas of the upgrade are:

- The reconstruction of about 16 beam-lines, with enhanced capabilities of nano-focusing the X-ray beam
- An upgrade to the accelerator complex, including longer straight sections to possibly increase number of beam-lines and, together with a newly designed lattice in order to improve the brightness
- Instrumentation developments, such as new X-ray detectors and nano-compatible machineries;
- Experimental hall to be extended to 21,000 m^2, permitting up to 16 beam-lines to be increased in length up to 140 meters, and to contain new infrastructure.

The upgrade programme strived to develop all areas of scientific research, however emphasis was given to five important fields:

- Nanoscience and Soft Matter;
- Structural and Molecular Biology;
- Pump-and-Probe Experiments and Time-Resolved Science;
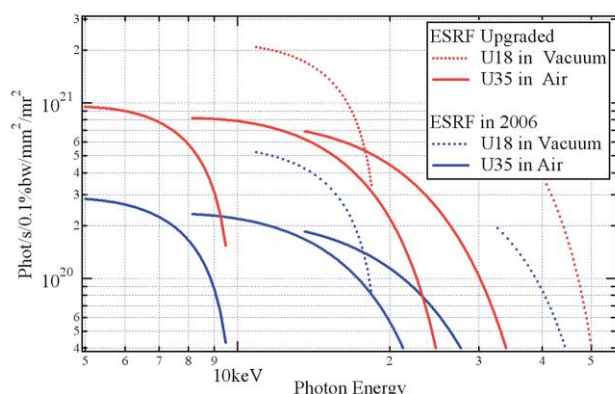- Science at Extreme Conditions;
- X-ray Imaging.

Figure 17: Comparison between brilliance from ESRF in 2006 and upgraded ESRF.[21]

Improvements in these fields were achieved by making fundamental changes to the engineering of beam-lines, as previously mentioned. The extension of the beam-lines provided more space for insertion devices to be installed in order to increase parameters such as coherence and brilliance. The brilliance was increased to 10^{21} photon $sec - 1mm - 2mrad - 20.1\% - 1bw - 1$, a feat made possible by installing 7m long straight sections, in which longer undulators could be implemented for each single beam-line. The beam coherence was also increased by a combined use of wigglers and undulators, resulting in beam stability close to 99%.

Intense heat load can affect the beam stability, lowering coherence. This was overcome by the use of canted and cryogenic undulators, which also resulted in the reduction of the vertical emittance. As a consequence, there was a large increase in the brilliance of the beam. Shrinking the vertical emittance not only increased the brilliance, but also reduced the focal spot size on the sample, allowing more sophisticated spatial resolution imaging techniques to be implemented. Having a small emittance can produce emittance fluctuations induced by the insertion device gap changes, which can cause a long response time. Skew correctors were therefore implemented to allow a stabilization of the vertical emittance by around 10 pm in all filling modes. These improvements, in addition to an increase of the current from 200mA to 300mA, increased the spectral flux by a factor of two. X-ray detectors were also substantially improved by introducing technologies such as hybrid pixel counting detectors with dynamic range mechanisms, as well as modern energy dispersive 2D detectors. The upgrade programme set the scenario for future upgrades to be implemented, as technological advancements surpassed real world engineering challenges[21].
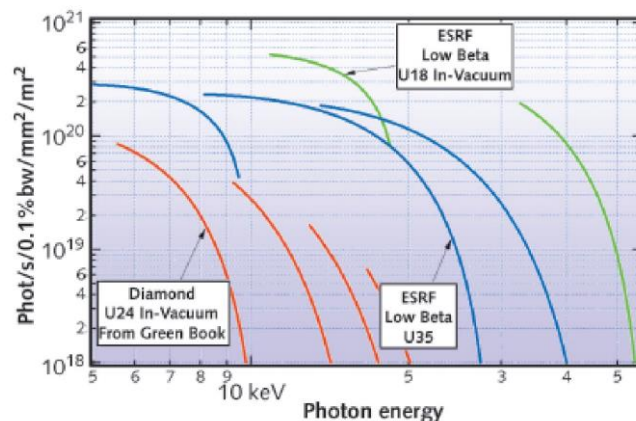

Figure 18: Brilliance in the hard X-ray range currently available at ESRF with 200 mA current compared to that of the Diamond Light Source at the nominal current of 300 mA.[22]

The 2008-2017 Upgrade Programme pushed the spatial resolution of the experiments from the micrometre to the nanometre range, thanks to the increasingly complex computational software for data collection and analysis. The programme plans to give users access to real-time analytical tools and more advanced data storage systems. Since the start of the programme, the number of user

requests for beam-time increased by approximately 20%. In 2017, the total number of proposals submitted increased to 2409, which was roughly 500 more than in 2015, indicating the successful outcome of the Upgrade Programme[23]. The ESRF Upgrade Programme facilitated advancements in a range of different fields. The field of medicine expanded investigations in their studies of molecular biology and pharmacology as a result of ESRF's improvement of nano-fluidics and optical tweezing[21]. In addition, investigations in experimental physics resulted in a deeper understanding of crystallography and solid-state processes. High-resolution IXS spectroscopy provided new opportunities in the fields of crystal lattice dynamics and electron-phonon interactions. Investigations at the ESRF, include the improved data collection techniques of anthropogenic drivers to study climate change factors[23].

PETRA III

Petra III is another accelerator project that took place between 2007 and 2009, with the aim of expanding the DESY Synchrotron facility in Germany as response to increasing demand from the scientific community. The previous Petra II 2.3km storage ring was enhanced into a third-generation high brilliance light source, which was achieved by replacing the FODO lattice with a DBA lattice, and improving the overall functionality of the insertion devices. Half of the DBA cell was supplied with 5m long undulators, while the other half was equipped with 2m long undulators. Strong sextupoles were put in place in order to correct chromatic aberration due to random dispersion of the beam. The radiation damping was also enhanced by damping wigglers, contained in the longer straight sections, which contributed to further reduction of the emittance. To compensate for the short lifetime resulting from this smaller emittance, the machine's injector complex was upgraded to run more frequent electron injections to the storage ring.

Petra III, with its 6 GeV beam energy and its new high brilliance of 2.0×10^{21} photon $sec^{-1}mm^{-2}mrad^{-2}0.1\%^{-1}bw^{-1}$ provided a range of different research opportunities. The higher flux combined with ultra-fast detector systems furthered global research in the field of electrochemistry, presenting opportunities to investigate the functionality of solid oxide fuel cells. In addition to advancement in solid state physics research options, current studies of molecular physics at DESY aim to improve the understanding of molecular rotation to reproduce novel meta-materials and optical devices in electronics and aviation. In 2012, an X-ray scanning microscope research group at PETRA III, announced that the upgrade was a necessary tool for the record spatial resolution of 10nm[24].

2.5.2 - Present Synchrotron Projects

The previous section explored the engineering challenges and solutions present in establishing third-generation synchrotron facilities. Theoretical growth combined with technological advancements introduced the new era of fourth-generation synchrotron facilities, which include ESRF-EBS, Elettra 2, Petra IV, SLS-2, APS-U.

ESRF-EBS project

The ESRF is currently the one of the most globally competitive Synchrotrons facilities, with a beam intensity of 6.04Gev and a brilliance of 8.0×10^{20} photon $sec^{-1}mm^{-2}mrad^{-2}0.1\%^{-1}bw^{-1}$.[25] To further reduce the horizontal emittance (increasing X-ray brilliance and coherence), a new lattice concept was developed in 2012, the 'hybrid multi-bend achromat' (HMBA) or Raimondi lattice. This lattice is quickly becoming one of the leading designs for future fourth-generation synchrotrons. With the reconstruction of the storage ring, ESRF aims to transform the X-ray source into a new 'Extremely Brilliant Source' (EBS). The project called, ESRF-EBS, intends to introduce a beam with ultra-low horizontal emittance in order to reach the experimental diffraction limit of 0.1nm[26]. The programme, in addition to replacing the existing storage ring with the new EBS low-emittance storage ring, also plans to establish new, adapted beam-lines with more advanced X-ray detectors. The ESRF-EBS programme was launched in 2015 and it is projected for completion in 2022.
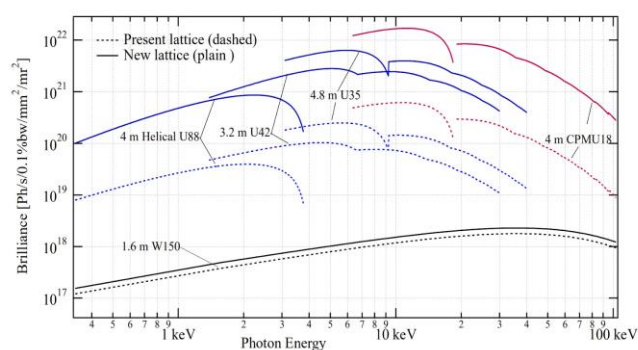

Figure 19: Comparison of beam brilliance between the new HMBA lattice and the old 3rd generation lattice.

As a result of the upgrade, the horizontal emittance is targeted to be reduced from 3.80 nmrad to 100 pmrad, which will produce an X-ray beam that is approximately 100x more brilliant than the current beam (figure 19). In addition the new HMBA lattice at ESRF aims to increase the coherence of the emitted beam by a factor of 20[27].
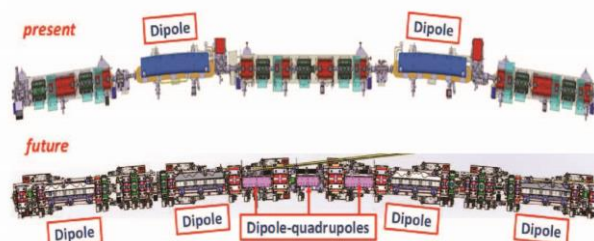

Figure 20: Layout of the existing DBA and lattice and the new HMBA lattice. [26]

Although the upgrade is aimed at increasing research opportunities in all fields, the scientific investigations at ESRF that will have a benefit most from the improvements include:

- Nanoscopy of new materials
- Structural biology and health sciences
- Materials science
- Nanotechnologies
- Environmental and energy sciences

This new fourth-generation synchrotron will therefore facilitate advancements in structural biology with the aid of a high-brilliance source, allowing the investigation of fundamental chemistry at atomic levels of detail. This will help open up new opportunities in catalysis and green chemistry. The ESRF-EBS programme will enable new research insights into quantum critical behaviour and allow for studies of materials at extremely low temperatures (in the range of superconductivity). With the fourth-generation synchrotron source, electrochemical processing of battery systems and photovoltaics can be investigated, easing the demand for 'greener' energy production[28].

MAX IV

MAX IV is the first synchrotron in the world to have upgraded its storage ring to the 'novel multi-bend achromat lattice'. This 4th generation Swedish project is characterised by the unique construction of two storage rings, which operate at two different energies. This allows the facility to cover a larger collection of spectral ranges[29].

The MAX IV facility was developed in response to concerns over the aging technical performances provided MAX II and MAX III. It became an urgent requirement to replace systems such as the injector complex, straight sections, and electron source, as these deteriorating constituents posed a high risk of breakdown during operations. The main part of the project concerned the replacement of the double bend achromat with the multi bend achromat (MBA) lattice, which involved 7 bending magnets (opposed to the 2 bending magnets found in the MAX III storage ring). In order to reduce the issue of beam instability and chromatic aberration, the sextupoles were added to the storage ring. The MBA lattice was employed in the 3GeV storage ring (high-energy ring), producing high brilliance hard X-ray radiation. The smaller 1.5GeV storage ring has the purpose of producing soft X-rays. This satisfies the large soft X-ray spectroscopy community in Sweden and meets the demand for further biological research.

The injector complex was improved by the use of the Linac and laser driven electron gun, which provides 100fs bunches in order to increase time based resolution of experiments. In order to achieve a stable constant beam flow, the storage ring will be operated in a 'top-up' filling mode, with injections every 2 minutes. This provides a lifetime of approximately 10h. The Linac length was also extended with, aims of expansion into a 'Free Electron Laser' in the future. The electromagnets, constituting wigglers and undulators, were replaced with permanent magnets that provide an alternating static magnetic field. Together with the upgraded insertion devices, the number of straight sections in the storage ring was also increased to 19[30].

The engineering improvements employed in the synchrotron drastically improved some of the parameters. The MBA lattice contributed to an ultra-low horizontal emittance of approximately 0.2 nmrad, which consequently improved the coherence of the beam. The use of longer insertion devices in the 19 straight sections, also contributed to an increase in the brilliance to a magnitude of about 10^{21} photon $sec^{-1}mm^{-2}mrad^{-2}0.1\%^{-1}bw^{-1}$.[25]

The MAX IV project was completed in the early 2018 and the enhancement of the facility showed incredible results in various fields of science. The higher degree of coherence, together with the extremely high brilliant beam, aims to approach the diffraction limit, reaching a scale that meets the academic demand in the fields of nano-science and nano-technology. Experimental improvements are not restricted to physical sciences but also biological and environmental sciences. The soft X-rays produced in the low energy storage ring are useful for investigating fields of macromolecular biology and structural biology, since molecular samples are not damaged by radiation-induced movements.[29]

2.6 – Coherent Diffraction Imaging

One of Diamond's primary applications is the imaging of nano-structures using 'Coherent Diffraction imaging' (CDI). This technique makes it possible to replicate the structure of an object to extremely fine levels of detail by analysing the diffraction pattern formed when x-rays pass through it.

2.6.1 - The Phase Problem

Recreating an object based off its diffraction pattern is made difficult by the nature of measuring diffracted waves. Diffraction patterns record the number of diffracted photons reaching a certain plane, resulting in a map of intensities. The nature of intensity means any phase information in these waves is not measured, resulting in a lack of the necessary parameters required to produce an image of the source object. This is known as the 'phase problem'.

The phase problem can be better understood by analysing the mathematical description of diffraction. Consider a wave incident on a slit of width greater than the incident wavelength (i.e. i.e. a>λ in figure n). The Huygens's-Fresnel principle states that 'each point on a wave-front is the source of an individual wavelet that propagates forward

with the same speed'[31]. This means that upon passing through the slit, the wave will spread out into the region of geometric shadow of the slit, and also interfere with itself to form a diffraction pattern. Each individual wavelet will interfere with 'adjacent' wavelets, resulting in maxima and minima at certain points beyond the slit as a result of constructive and destructive interference.

Constructive interference will occur when two interfering wavelets are in phase (i.e. the distance travelled by protruding wavelet is an integer multiple of the other), and destructive interference will occur when they are out of phase. It is simpler to determine at what point the wavelets are in or out of phase by considering each propagating wavelet to be completely parallel at the point of interference, as shown in figure 21.
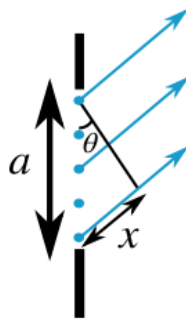
Figure 21. An illustration to show the path difference, x, that a photon diffracting at the bottom slit would gain in comparison to a photon diffracting at the same angle from the top of the slit.

Although it is impossible for wavelets propagating parallel to each other to interfere, when considering points in the 'far field' (i.e. when the distance from the slit is significantly greater than the wavelength of the wave), they may be approximated as so. This is known as the 'far field approximation' or 'Fraunhofer Diffraction', and it will be applicable to all relevant examples henceforth.

From figure 21, it is evident that constructive interference occurs at the point where $x=a\sin\theta=n\lambda$. This thinking can be extended to consider the interference of all infinitesimal wavelet points passing an aperture. Considering that interference of two wavelets results in an amplitude equal to the vector sum of the initial waves, a proportionality can be derived to consider the complex amplitude of a diffracted wave at a certain point from the slit, in Cartesian space:

$$A'(x,y,z) \propto \iint A(x,y)e^{-ik(x+y)}dx\,dy$$

Where A' refers to the scattered amplitude and A the amplitude of the incident beam, x and y are the coordinates on the sample that the beam has diffracted off of forming a source of wavelets and k the wavevector the beam.

This equation is known as the Fraunhofer Diffraction Equation. With respect to its derivation, it is only applicable

in the 'far field'. Inspection of the Fraunhofer Diffraction equation shows the respective integral to be equivalent to the Fourier transform of the aperture/transmission function at certain frequencies, allowing it to be re-written as:

$$A_{scattered}(\vec{r}) = \int T(\vec{r})A_{incident}(\vec{r})e^{(-i\varphi(r))}d\vec{r}$$

Where $T(r)$ is the transmission function, $A_{incident}$ the amplitude of the incident beam at the sample, $A_{scattered}$ the amplitude of the scattered beam at the detector and $\varphi(r)$ the phase of the beam.

In order to reconstruct an image of an object, the transmission function must be found. The transmission function describes the nature of the diffracting object (for example, in the case of photons diffracting from a crystal lattice, the transmission function describes the electron density of atoms in the sample). Inspection of the Fourier transform shows that taking an inverse Fourier transform of the scattered amplitude would allow the transmission function to be determined, given that the incident amplitude at the slit (and the phase information) is known. The scattered amplitude can be determined through measurements of the square root of the intensity provided by a diffraction pattern. However, as described previously, the phase information cannot be found from the diffraction pattern intensities alone.

2.6.2 - Phase Retrieval Algorithms

The phase problem can be solved by the application of an iterative feedback mechanism, or 'phase retrieval algorithm'. The application of these algorithms, also known as the 'oversampling method', is used to find the phase of a beam without a direct measurement of the beam's phase ever being made.

For the oversampling method to be valid, a condition known as the oversampling ratio must be obeyed. This states that for an n dimensional space, the sampling ratio (as stated below), must be greater than $2^{(1/n)}$. If this is true the phase can be retrieved from this approach[32]:

$$\sigma = \frac{\text{electron density region} + \text{no-density region}}{\text{electron density region}}$$

Where σ is the oversampling ratio and the 'region' represents the pixels in the image that contain an electron density. This method has various applications, but most importantly it can be applied in CDI for a 2-dimensional diffraction pattern.

In the phase retrieval algorithm, there are two main classes of algorithms: the 'Error-reduction algorithm' (ER) and the 'Hybrid input-output algorithm' (HIO). The ER algorithm is a general form of the 'Gerchberg-Saxton' (GS)

algorithm[33], a phase retrieval algorithm that requires knowledge of the phase of either the sample or intensity distribution. The ER algorithm operates using a source intensity distribution, formed due to the scattered incident EM radiation off a sample. It applies an Inverse Fourier Transform to receive a random phase and an approximate image of the sample. A Fourier transform is then applied to the generated phase and incident amplitude of the EM beam at the sample, producing an approximate intensity pattern, known as a hologram.

The iteration process for the ER algorithm operates by evaluating the Fourier-domain constraints (which apply boundary conditions to ensure that the generated intensity distribution has the same amplitude as the original intensity distribution at all points) and the object-domain constraints (which ensure that the dimensions of the sample and the approximated sample are the same). Once both criteria have been satisfied, the iterations converge to a minimum solution between the generated sample and the original sample[34] (measured by determining the chi-squared value between the generated sample and the actual sample).

Complications of the ER algorithm include the stagnation problem and the convergence problem[35]. The stagnation problem refers to the situation where the algorithm tends to a minimum before finding the global optimal solution. This can occur when the boundary conditions are falsely flagged positive. For instance, truncations of the image's dimensions by the support constraint can lead to an 'optimal' result (due to the precision of the code), and so need to be closely observed. The convergence problem occurs when the algorithm tends to a local minimum rather than a global minimum. In the process of reconstructing the phase, many local minima can exist depending on the initial conditions (such as the random phase that is used to start the loop). Since ER always reduces the previous errors, it will easily converge to a local minimum rather than the global minimum if boundary conditions are not set appropriately. For both these issues, a large amount of time is necessary to distinguish whether the code has accurately reached a global minimum. Furthermore, to produce highly accurate images of the sample, a large number of iterations are required, increasing the likelihood of the code stagnating.

The HIO algorithm is an extension of the ER algorithm[36]. It applies to only the Fourier-domain constraints and ignores the object domain constraints by applying a negative feedback algorithm in the Fourier space. The HIO algorithm is strictly enforced to improve the Fourier domain, greatly increasing the accuracy and speed of the iterative process by providing a more accurate hologram to iterate from. This means that when an inverse Fourier transform is applied, the algorithm generates a more accurate sample image in the real domain and so improves the efficiency of the code (by reducing the risk of stagnation as the code always seeks the most optimal fit).

The HIO algorithm requires less iteration due to the Fourier and object domain being constrained. This requires less computational power per iteration.

When HIO is used in conjunction with ER it significantly reduces the likelihood of the algorithm iterating at a local minimum rather than the ideal global minimum. However, care must be taken on the strength of the negative feedback parameter, as HIO can produce mirrored images of the original sample and also exceed the global maximum, resulting in inaccurate images. Furthermore, an iterative algorithm that only applies HIO constraints will never converge to a minimum and will never produce an optimal solution. Hence, applying both the HIO and ER algorithms together will greatly reduce errors, compared to if the algorithms are applied independently.

Other methods have also been developed to resolve the phase problem, such as the Hybrid projection-reflection method, which improves the efficiency of the algorithm's convergence. These algorithms are fundamentally built upon the ER and HIO algorithms. Visualizations to illustrate how the ER, HIO and ER combined with HIO algorithms operate can be seen in figure 22:
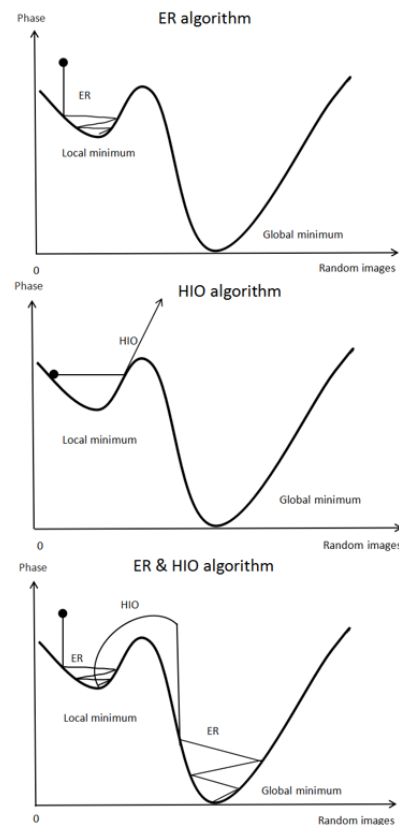

Figure 22. illustrations demonstrating how both the ER and HIO algorithms iterate across potential generated images to return optimal solutions

2.6.3 - Bragg Coherent Diffraction Imaging

A specialization of CDI known as Bragg Coherent Diffraction Imaging (BCDI)-also implemented at Diamond-applies CDI in Bragg geometry. BCDI is simply CDI for diffraction in which Bragg's Law may be applied (e.g. diffraction from lattice vectors). For BCDI a unique phenomenon occurs for incident x-rays of wave-vector, k, that has parallel components to the reciprocal lattice vector, G, that are half the magnitude of G. In this case the incident x-ray's wave-vector is said to terminate in reciprocal space at what is known as the 'Brilloiun zone boundary'. This implies that the incident x-ray satisfies Bragg's law, and so will be diffracted/ scattered characteristically.

3 - Method

Before coding the CDI algorithm, it was decided that we should first understand how to code an electromagnetic wave diffracting in one of the simplest models known, the young's double slit experiment. Taking the average photon energy of the I13-1 beamline's 6-20keV range an estimated value of the wavelength of the coherent ideal x-ray beam was calculated:

$$E = hf = \frac{hc}{\lambda}$$

Where E is the energy of the beam for a single photon, f the frequency of the photon, h the planck's constant and λ the wavelength of the photon.

A 2-dimensional array was generated to plot an intensity-position value in both the y and x axis by using a sinusoidal wave equation. After the array was created boundary conditions were imposed for the locations of the virtual double slits. This resulted in the free wave fronts, as seen by the vertical lines on the left-hand side of the images in figure 23, diffracting at these locations resulting in the formation of an intensity pattern at a detector (the far-right side of the image). The angle from the slit that maxima and minima would form was determined by the young's double slit formula as shown in the in the following equation:

$$\theta = \arcsin\left(\frac{m\lambda}{d}\right)$$

Where d is the displacement between the double slits, λ the wavelength of the incident photons and m a constant that is an integer for constructive interference at the detector and half an integer for destructive interference at the detector.
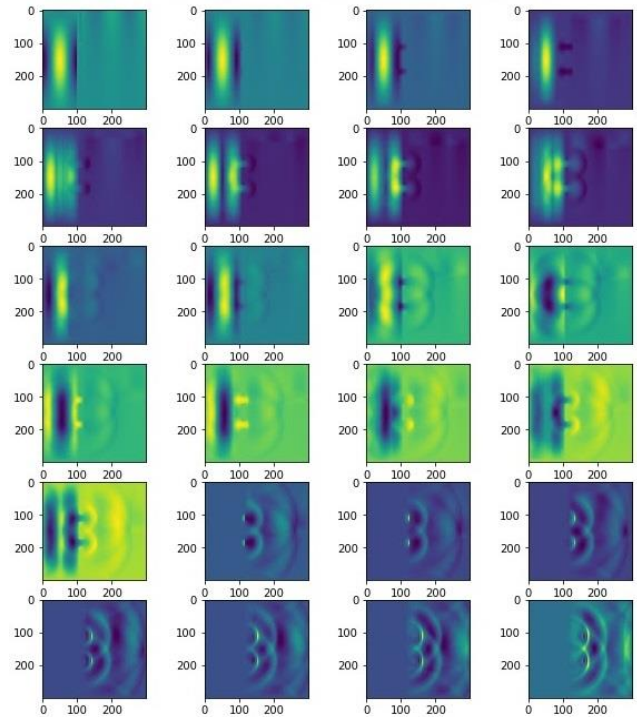

Figure 23: intensity map of a wave propagating and interfering in the Young's double slit experiment. Each image is a set increment of time after the previous one starting from the top left and ending at the bottom right.

The progression of the wave fronts was then visually shown through a colour map of the intensity-position values that updated at set increments in time as shown in figure 23. After successfully mapping the intensity distributions for the double slit case, consideration into how to apply a similar coding mechanic into a CDI distribution was considered. It was determined that the level of coding required to accurately plot the wave diffracting off a 2-dimensional sample was far too challenging and so was substituted for a more refined model that involved applying the Fourier transform on the sample to generate the intensity distribution. Nevertheless, the insight gained from generating a 2-dimensional wave front and understanding issues that may arise due to asymmetries at the slit locations was critical for the later stages in the coding task and so was seen as a beneficial endeavour.

The process of creating a computational model for the CDI experiment in Diamond I and Diamond II was split into 3 main sections. The first task was to successfully retrieve the phase information (and thus image a sample) from an intensity distribution for a coherent x-ray beam. To simplify the earlier models of the code we would begin with a simple sample image with uniform electron density. The simplified sample consisted of 4 square lattices that each contained 1000 atoms (modelled by array points) containing an electron density charge of plus minus 1.6 times 10^-19 coulombs with the plus minus sign for each square shown in the legend. This was created to treat array

points/ pixels as infinite square wells binding the electrons to discreet locations.

A discrete Fourier transform was then applied onto the electron density of the complete sample to retrieve the scattered amplitude of the diffracted radiation and a value of the real phase that can be used to reconstruct the intensity distribution at the detector. This phase information was then ignored to mimic the phase problem that occurs in real experiments. The oversampling method was then initiated, and a measurement of a random phase was generated between 0 and 2 pi. An inverse Fourier transform, is applied on the scattered amplitude and the random phase, as explained in theory, to receive the electron density resulting in a new reciprocal space image of the sample lattice.

The new sample image will be distorted from the original sample due to the phase being random and thus incorrect. To correct this a comparison between the original sample and the generated sample is performed through an ER algorithm by applying constraints in the object (sample) domain. The ER boundary conditions constrained the new sample image by noting areas in the original sample that had an electron density of 0 and ensured this to be also true in the new image. The ER boundary conditions also ensured that the dimensions of both the real and generated samples were the same.

A Fourier transform is then applied on this sample to retrieve a new intensity distribution which will then undergo Fourier-domain constraints by applying either the HIO or ER algorithm. The Fourier domain constraints ensured that the new "real" phase calculated from this Fourier transform satisfies the domain constraints i.e. the samples size, as well as that the magnitude of the intensity (scattered amplitude squared) is the same as the original intensity distribution. After being constrained the new intensity distribution will then have an inverse Fourier transform applied to it to retrieve another new sample image. An illustration of the oversampling method can be seen in figure 24 to give a visual representation of the algorithm that was coded.
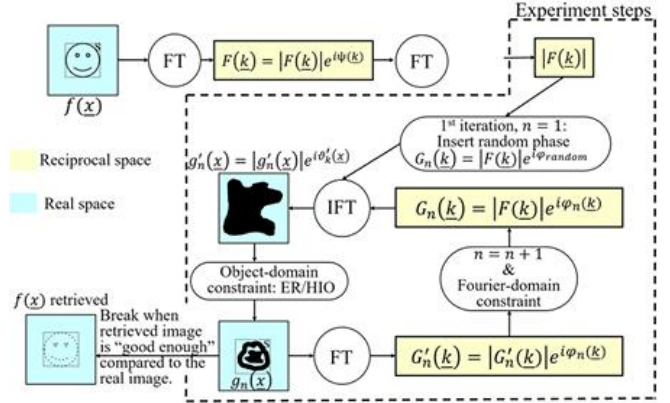

Figure 24: illustration of the oversampling method to give a visual understanding of each iteration loop and the logic gates that are applied in the code.

This process iterates and constrains the samples in both the real and reciprocal space until the chi square value, as calculated with the equation below, between the created intensity pattern and the generated intensity changes a trivial amount per iteration (for this experiment it was chosen to be 0.001.).

$$X_{image}^2 = \frac{\sum \left| n_{retrieved}(\vec{r}) - n_{original}(\vec{r}) \right|}{\sum \left| n_{original}(\vec{r}) \right|}$$

$$X_{intensity}^2 = \frac{\sum \left| I_{retrieved}(\vec{r}) - I_{original}(\vec{r}) \right|}{\sum \left| I_{original}(\vec{r}) \right|}$$

Where X denotes the chi square between the real (original) and generated (retrieved) object and Fourier domains respectively.

 Once the chi-square limit was reached the final generated sample from the oversampling method for coherent x-ray beams was plotted against the number of iterations taken to reach this point. During this process it was noted that varying the ratio of how often either the ER or HIO algorithms occurred had an impact on the accuracy of the generated sample as well as the number of iterations required to run the code. This is due to aforementioned dilemmas caused due to how algorithms apply boundary conditions and so the code was optimised through careful changes to the parameters to ensure that the final generated image was not only the most accurate image but also minimised the number of iterations required to reach the global minimum chi-square value.

The second task was to model the CDI experiment with an incoherent incident x-ray beam. We first began by considering both the variation in the longitudinal and transverse coherence. As seen in figure 25 the longitudinal coherence causes incoherent wave fronts in the x ray beam due to slight differences in each photon's wavelength with

this change in wavelength being calculated as shown by the following equation:

$$L = \frac{\lambda^2}{2\Delta\lambda}$$

Where λ is the wavelength of the wave front, **Δ** λ the change in wavelength between each wave front and L the displacement that two in phase wave fronts travel before becoming out of phase with one another due to their longitudinal incoherence.

The level of transverse coherence is dependent on the x-ray beams wave fronts being at slightly different angles to one another as they travel towards the sample. This means that at certain locations the wave fronts, even if longitudinally in phase, will interfere with other wave fronts. Furthermore, the individual wave fronts will diffract at slightly different angles to the ideal coherent case contributing to al lower.
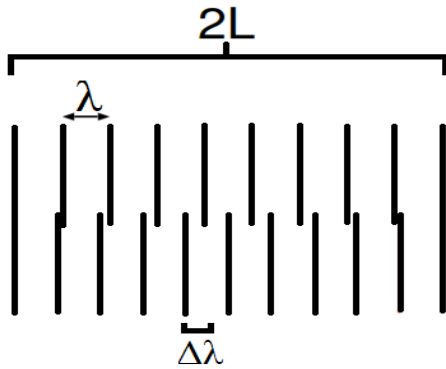
Figure 25. illustration of longitudinal incoherence between two waves, one with wavelength λ and the other with wavelength λ+ Δλ.

Accounting for this incoherence we modified our discrete Fourier transform as follows:

$$\Gamma(\boldsymbol{Q}) = \int \gamma(\boldsymbol{r}_\perp) \, C(|\boldsymbol{r}_\parallel|) e^{-i\boldsymbol{Q}\cdot\boldsymbol{r}} \, d\boldsymbol{r}$$

Where the new term, γ, accounts for the incoherence in the beam based off the beams emittance and is equivalent to:

$$\gamma_{in}(r_\perp) = e^{\left(-\frac{x^2}{2\xi_x^2} - \frac{y^2}{2\xi_y^2}\right)}$$

Where x and y are the beam's perpendicular components on the sample with x and y corresponding to a position in space, ε x and ε y represents the two transverse coherence lengths and are equivalent to the following:

$$\xi_{x,y} = \frac{L}{(k\sigma_{x,y})}$$

Where L is the distance between the sample and the detector (for diamond this is approximately 250m), k the average wave vector at energy 8kev and σ represents the halfwidths of the intensity distributions and is made from the root product of the emittance (in the respective x and y

plane of the beam) with the undulators magnetic focal length. For coherent light the beam's emittance tends to 0 and so this gamma factor tends to 1 thus by using Diamond I's measured values and Diamond II's predicted values for the vertical and horizontal emittance we are able to create an accurate representation for the incoherent beam.

Finally, once the simple pixel sample was successfully retrieved when using both the coherent and incoherent incident X-ray beams a more complicated sample was used to mimic more realistic samples that would be more likely to occur at the facility. This was implemented by setting the sample pixels to a finite potential well where neighbouring pixels would have a fraction of the original sample's electron density. This is because in quantum mechanics, the electron density is equal to the probability density function for an electron to occupy an infinitesimal element around any point in space. This resulted in a density map of the electron charge that does not purely exist at discrete locations but would be continuous to mimic a crystal lattice and so would represent Braggs coherent diffraction imaging more accurately. To achieve this the model applied a continuous sinusoidal function based off of a two-dimensional cross section of an fcc lattice. Instead of treating the pixels as discrete infinite square wells

 After we had created both the pixel and continuous sample spaces, we then began to test the iterative CDI algorithm on more complicated symmetries then the previous square samples. To do this an algorithm was devised that loaded images and converted them into black and white images with a grey scale going from 0 (white) to 1 (black) where we have programmed pixels with a grey scale of 1 to have a maximum electron density, set as , and 0 to have no electron density. From this we were able to successfully model the samples however, we had originally noticed that the replicated images formed from the CDI method resulted in mirrored reflections if the sample image was asymmetrical. To model the antisymmetric cases a simplified GS algorithm was applied to generate images of the samples. This model is significantly less accurate than that of the ER and HIO approach as it cannot retrieve the phase information however can reconstruct the sample to a certain accuracy.

4 - Results and Analysis

4.1 - Double slit diffraction

Figure 26 describes the field amplitude of slits in complex space against position, thus the model can be treated as a one-dimensional system. The field amplitude is 0 everywhere except the two gaps in the middle and the values are 1 v(μm)^-½ after the normalization. This is because the simulated beam can only pass through the slits and is reflected elsewhere by the simulated barrier. Therefore, this figure has demonstrated the density distribution of a 1-dimensional slit and it corresponds to the

density distribution of samples in all of the following sections.

A Fourier transform of the electron density distribution of the slits forms a diffraction pattern in the reciprocal space which can be seen in figure 27. The pattern has sine and cosine waves behaviour which match with the theoretical results of double slit experiment. Thus, the application of Fourier transform can be applied in the following sections where the cases of 2-dimensional diffraction patterns are discussed.
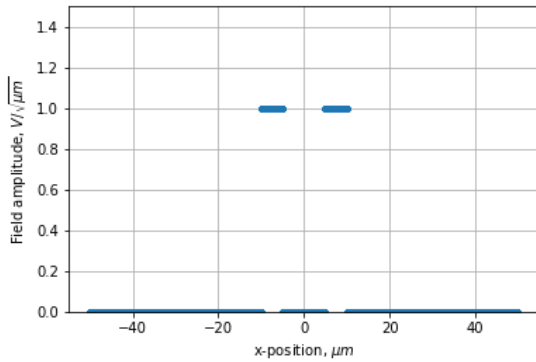

Figure 26: plot of the double slit experiment in a 1D complex field against a 1D real space. The field amplitude is in a complex field with unit v(μm)^-½, and the x axis has units μm. The width of the slit is 5 μm.
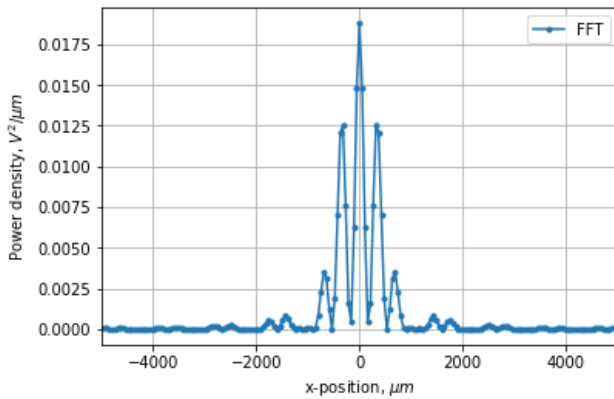
Figure 27: An intensity pattern of a double slit experiment in the 1D complex field against the 1D real space. The field amplitude is in a complex field with unit v^2(μm)^-½, and the x axis has units μm.

4.2 - Coherent Diffraction Imaging (CDI)

4.2.1 - Coherent X-ray beams

a) Oversampling ratio = 9

The algorithm modelled the simulated incident X-ray beam to be both coherent and normalized. This is the simplest case because the intensity distribution of the diffraction pattern has no dependency on the characteristic features of the incident beam, and it can be found by the Fourier transformation of the sample's electron density directly. From calculating the value of the oversampling ratio which was found to be 9, This is above root 2 and so meant that we could apply the oversampling method in our 2D case as well retrieve the phase information of the beam.

To start the model in the simplest manner, a square sized sample which is comprised of 100 by 100 pixels and has a uniform electron density distribution of 1 v(m)^-½, was placed in the centre of a low-density background space of dimensions 300 by 300 pixels. Another assumption that was made was that the initial phase of the beam was set to 0. As shown by the figure 28, the sample has been retrieved after 24 iterations through the code of ER and HIO algorithms. The retrieved phase has a symmetry property which can cause the symmetry problem that will be discussed in the section 2.6 and can be seen in figure 29.
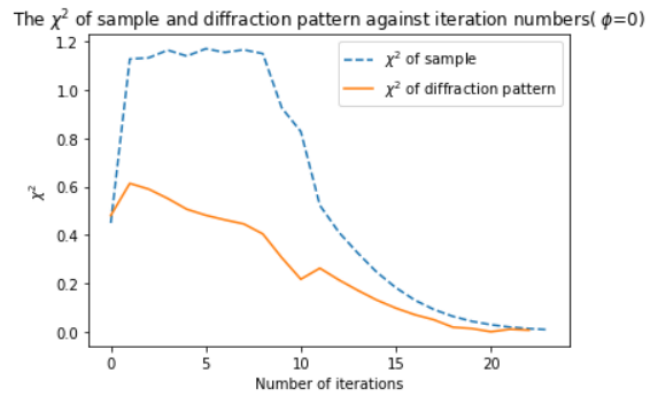

Figure 28: The chi square of the sample and diffraction pattern against iterations when the initial phase is equal to 0.

The chi square graph is plotted to show the similarity between reconstructed and original configurations of both the sample and diffraction pattern. In figure 28, the chi square of the sample has risen from 0.4 to 1.2 after the 1st iteration and it fluctuates around 1.2 until the 8th iteration. This phenomenon is due to the application of HIO algorithm which increases the difference between two adjacent images to allow the chi square value "jumping" out of the local minimum. From the 8th iteration till the 24th, the chi square of the sample decreases exponentially to 0.01 due to the ER algorithm. The decline of the chi square of the diffraction pattern is less dramatic, because it almost decreased linearly apart from the 2 small "jumps" at the 1st and 10th iterations due to the HIO algorithm.

Figure 29 displays the sample image reconstruction from a diffraction pattern caused due to an incident coherent X-ray beam illuminating the sample. Although this case was purely theoretical as currently there is no way to generate perfectly coherent x-ray beam, it was extremely useful to test the capability and the efficiency of the computing model.
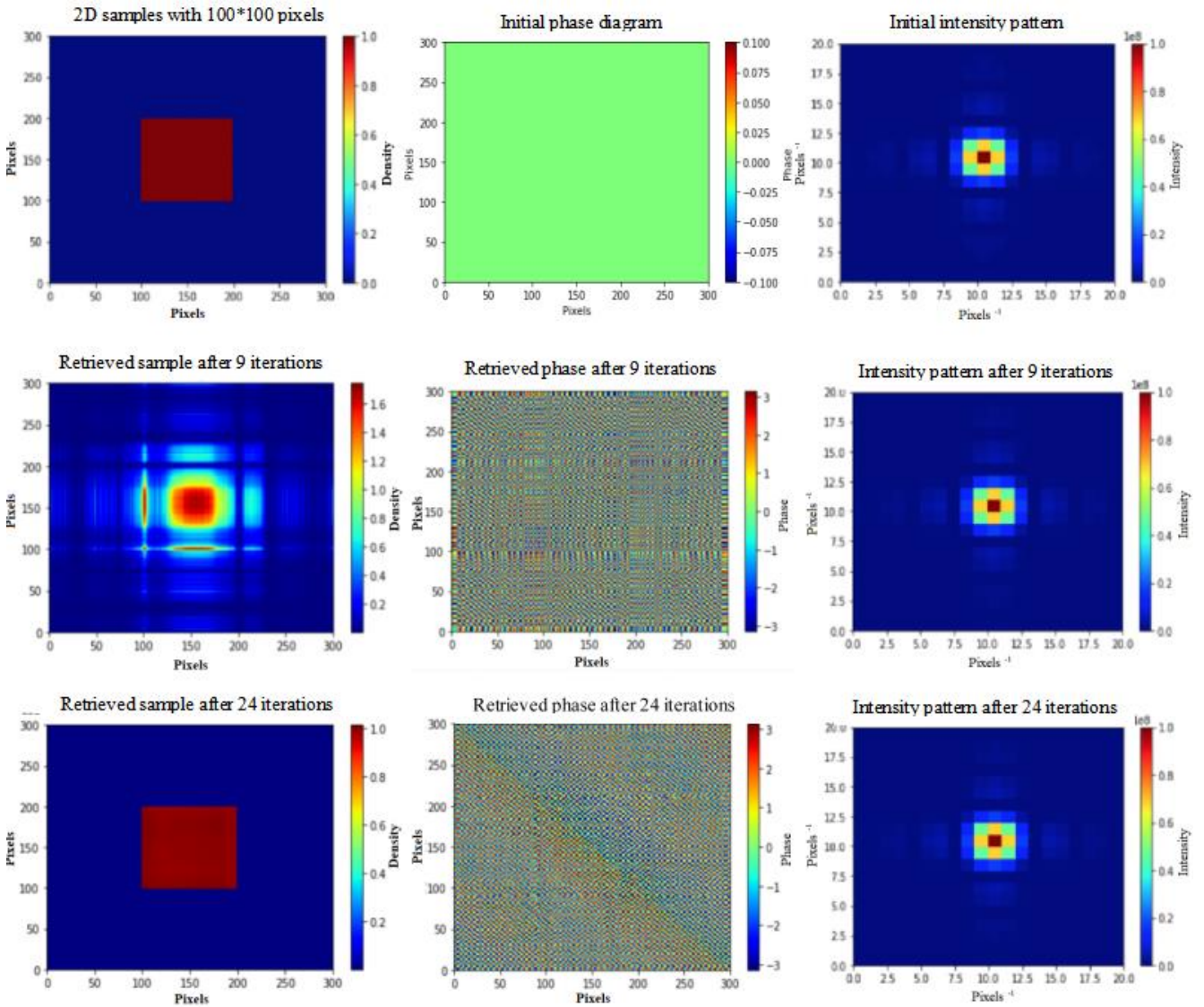
Case 1 : Φ = 0

Figure 29: The first row of diagrams shows the original sample, initial phase diagram and the initial intensity pattern. The second row shows the recovered sample, retrieved phase and the reconstructed intensity pattern after 9 iterations. The third row shows the final results after 24th iterations. The sample is given as a square with lengths of 100 by100 pixels and an oversampling ratio is 9.
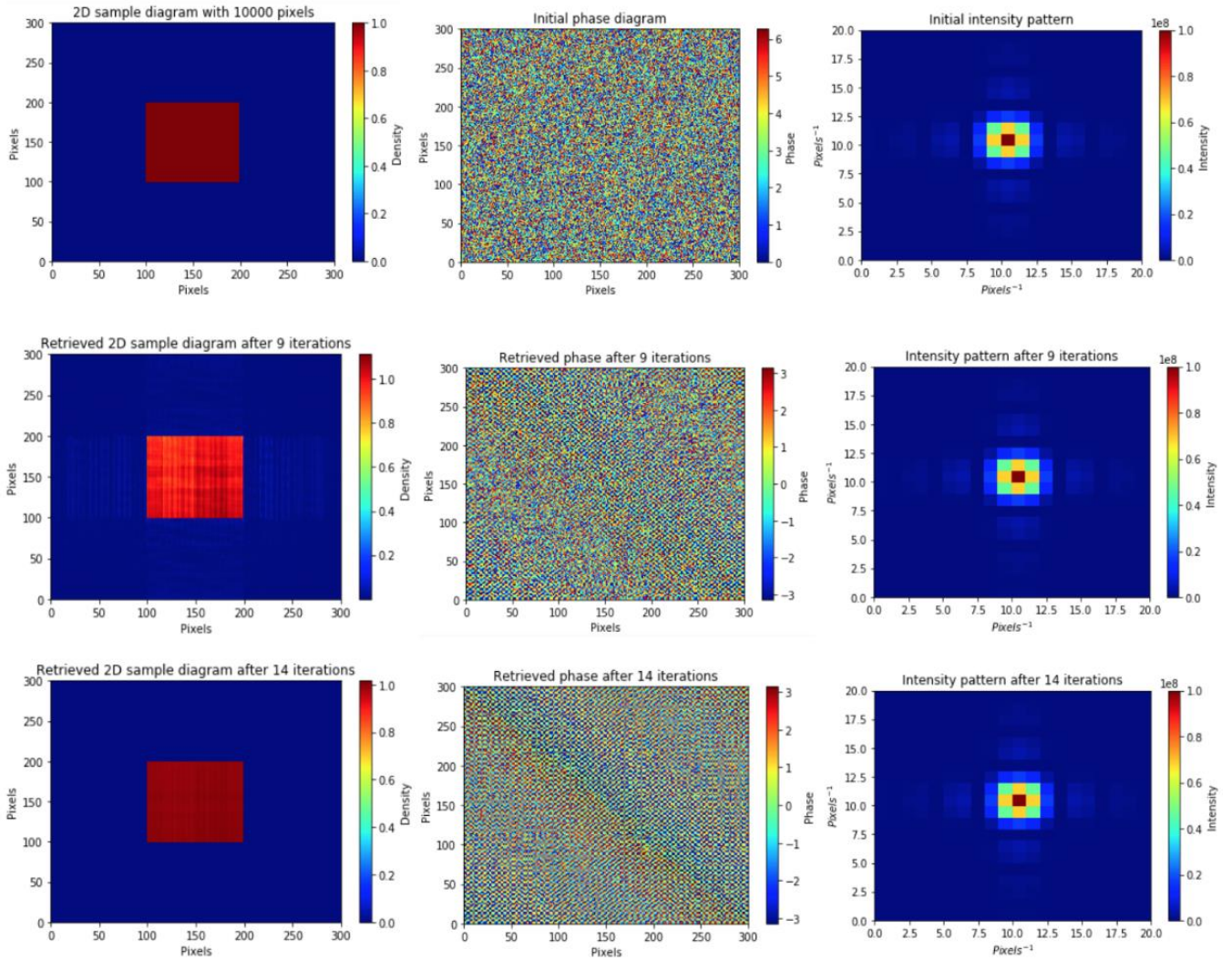
Case 2 : Random Φ

Figure 30: the first row of diagrams shows the original sample, initial phase diagram and the initial intensity pattern. The initial phase diagram is random in this case. The second row shows the recovered sample, retrieved phase and the reconstructed intensity pattern after 9 iterations. The third row shows the final results after 24th iterations. The sample is a square with 100 by 100 pixels and the oversampling ratio is 9.
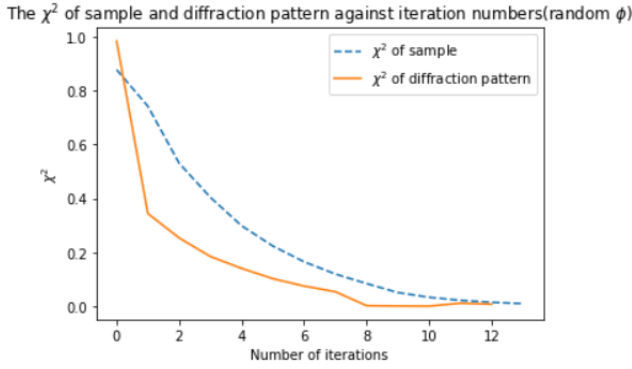
Figure 31: the chi square of the sample and diffraction pattern against iterations when the initial phase is random.

Figure 30 uses the same sample as figure 29, with the only difference being the random initial phase. This would result in a recovered sample with random density distribution after the 1st iteration. Then, the ER and HIO algorithms are implemented together to reconstruct the sample until it becomes the original one.

A surprising result of the reconstruction is the successful recovering of the original sample after the 14th iteration. This result has 10 iterations less than the previous one which had an initial phase equal to 0. As shown in figure 31, the chi squared curves of both the sample and the diffraction pattern decrease smoothly with very little amount of "jumps". As a result, the HIO algorithm was not applied and the ER algorithm reached the system minimum on its own. This implies that the algorithm runs faster by introducing a random initial phase. After hundreds of tests, the number of iterations were found to vary between 14 and 24 as the amount of iterations is dependent on the initial value of the phase. In conclusion, setting the initial phase to be a random value can improve the efficiency of the code. However, a drawback of using random phase initially can affect the initial value of the chi squared of the sample because the first sample pattern will always be distributed randomly.
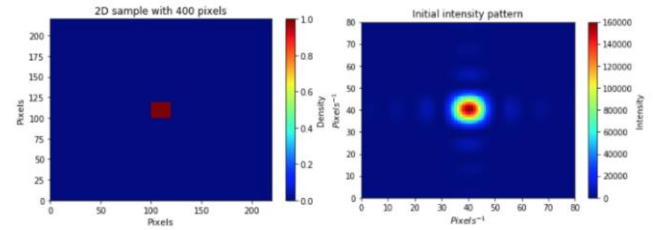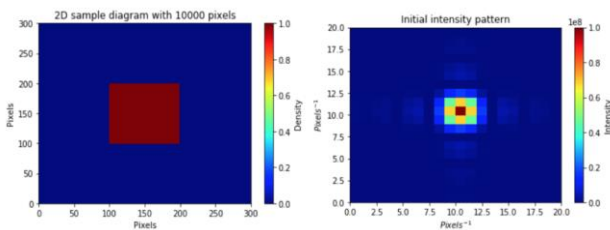
b) Oversampling ratio = 121

Figure 32: The first row shows the original sample and the intensity pattern with an oversampling ratio of 9. The second row shows the original sample and the intensity pattern with an oversampling ratio of 121.

In this section, the relationship between the quality of the diffraction pattern and the oversampling ratio is going to be discussed. The sample size has been decreased hugely compared to the sample with oversampling ratio equals to 9. The oversampling ratio of this smaller sample is 121. In addition, it was produced with 20x20 pixels. (See Appendix A.1 for the full results of phase retrieval test.)

In figure 32, the intensity patterns of the two samples are distinguishable. Firstly, the intensity pattern of the sample with an oversampling ratio equals to 9 has discrete intensity properties. Due to a small amount of pixels, the change of intensity around the boundary of the pixels is very clear. For example, the value of integration will be more precise if the object is divided into smaller pieces. Therefore, the intensity pattern around the boundary undergoes a clear change of pixels and the fluctuation of the intensity is lost.
When the oversampling ratio is bigger, the intensity pattern becomes more continuous and clear. The improved quality of diffraction pattern is due to the increased pixel numbers, so small changes in intensity are detectable. If there is an infinite amount of pixels in a diffraction pattern, the quality of the graph would increase and it will have continuous change in intensity.

Overall, increasing the sampling ratio improves the quality of the diffraction pattern as it retrieves more information on the variation of the intensity. However, reconstructing the best intensity patterns is not the aim of the project. In addition, code runs faster with smaller oversampling ratios due to less iterations. For the sake of simplicity, the oversampling ratio of the sample will be kept at 9, for future calculations.

4.2.2 - Incoherent X-ray beams

In this section, the coherence of the X-ray beam is studied. When the beam is entirely coherent, the amplitude of the beam shining through the sample can be a constant. In section 4.2.1, the amplitude was normalized to be 1 and the intensity of the diffraction pattern depends on the density of the sample entirely. However, when the beam is incoherent, the intensity of the diffraction pattern depends on the light amplitude upon the density distribution of the sample to make the model more complicated. To simulate X-rays which are as similar as possible to real beams, the following model has adapted the beam energy from I13 in Diamond which is 8000 eV.

a) Testing the model

Case 1 : σ x = σ y

χ^2 limits	σx (m)	σy (m)	Iterations
1e-3	1	1	72
1e-3	1e-1	1e-1	29
1e-3	1e-2	1e-2	17
1e-3	1e-3	1e-3	17

Table 3: table shows the relationship between the sigma value and number of iteration for phase retrieval test. The chi square limit of reconstructed and initial diffraction pattern is set to be 1e-3. The values of sigma x and y are the same.

Sigma is a measurement of the half width of the Gaussian spread of the intensity distribution. The sample studied is a 100x100 pixels square with oversampling ratio 9. The initial phase is set to be a fixed number 0, for each test since the number of iterations depends highly on the initial phase. When sigma is 1 m, the X-ray beam is very incoherent, thus it takes 72 iterations for the reconstructed diffraction pattern to match with the original diffraction pattern. The numbers of iteration decrease exponentially by decreasing the value of sigma which results in making more coherent beams. The number of iterations stops decreasing after sigma equals 1e-2 m. This means the decrease in sigma after such value will not result in a better reconstructed diffraction pattern. However, a potential problem with this model is the high value of the chi squared limit of the diffraction pattern which is 1e-3. In the later section, this value is changed to 1e-8 to compare the results from the experiment in Diamond I and Diamond II.

An alternative way to see the effect of decreasing sigma on the phase retrieval, is by observing the final reconstructed sample. In appendix A.2, when the X-rays illuminate the original sample more coherently, the final reconstructed sample will appear more alike to the original sample. For instance, the reconstructed sample does not have a square shape as the original sample when sigma is 1m, whereas, when σ is 1e-3 m, the reconstructed sample appears the same as the original one.

Case 2 : σ x ≠ σ y

χ^2 limits	σx (m)	σy (m)	Iterations
1e-3	1e-1	1e-1	29
1e-3	1e-1	1/∞	17
1e-3	1e-1	1	72

Table 4: table shows the relationship between the sigma value and number of iterations for phase retrieval test. The chi square limit is set to be 1e-3. The value of sigma x is fixed at 1e-1(m), while the sigma y values vary with 3 values, namely, 1e-1(m),1/∞(m)and 1(m).

The x component of sigma was kept constant, whilst the value of the y component was varied. According to the table, the amount of iterations to recover the diffraction pattern is highly correlated with the y component of sigma. The amount of iterations for sigma y to be negligible is 17 as this is the same as the ideal case. There are 72 iterations when sigma y is 1m, in order for the diffraction pattern to finish the reconstruction.

Moreover, the pattern of the retrieved sample is related to the complex degree of coherence(CDC) which describes the coherence of the incident X-ray beams (see appendix A.3.).

When the values of both sigma x and y are in the order of 1e-1m, CDC has a circular shape with radially decreasing intensity away from the centre. The retrieved sample has varied density which distributed in a similar fashion to the intensity pattern of CDC of the sample. For the case that the sigma y is negligible, CDC has maximum intensity horizontally across the middle of the sample, and it linearly decreases to the edge of the sample. Therefore, the retrieved sample has the highest density crossing the middle of the sample and the lowest along the edges. When the value of sigma y is equal to 1m, the pattern of CDC is squashed into an ellipse which has intensity vertically distributed at the centre of the sample. As a result, the retrieved sample has a vertical density pattern through its centre.

b) Comparison of Diamond I & II

	χ^2 limits	σx (m)	σy (m)	Iterations
Coherent X-ray	1e-8	1/∞	1/∞	49
X-ray from Diamond I	1e-8	2.509e-6	1.329e-7	49

X-ray from Diamond II	1e-8	5.611e-7	1.329e-7	49

Table 5: a comparison of the reconstructed diffraction pattern between the coherent X-ray, X-ray from Diamond I and Diamond II. The chi square limit for diffraction pattern is 1e-8, and the number of iterations are all equal to 49.
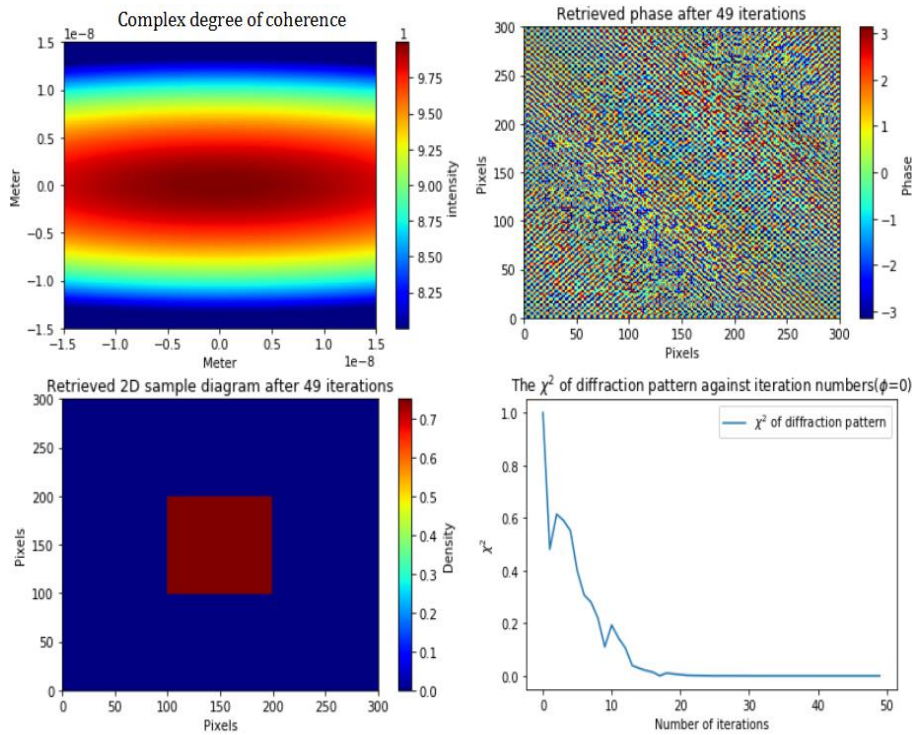
Diamond I
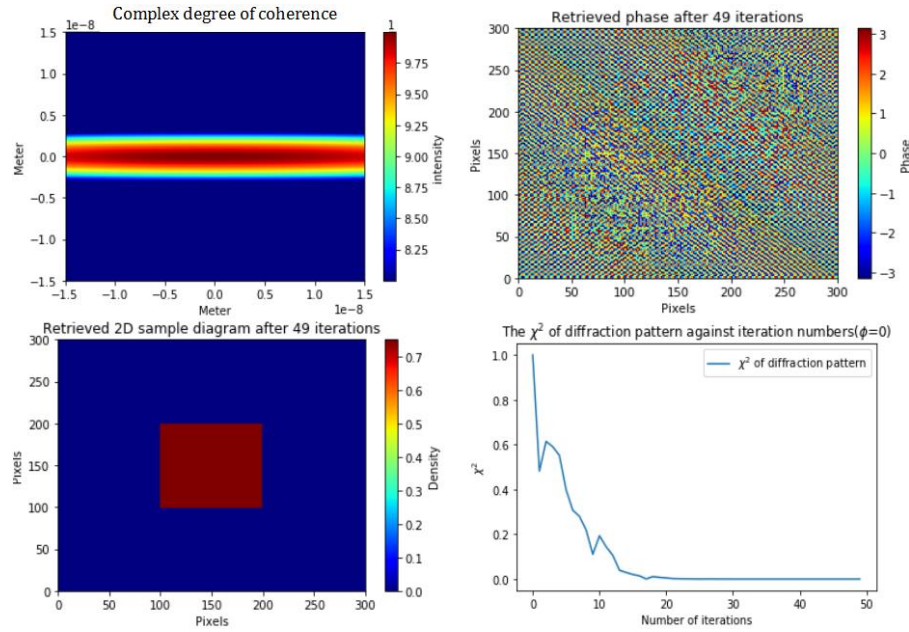
Diamond II

Figure 33: Graphs of CDC, reconstructed sample, retrieved phase, chi squares against iterations for both Diamond I and Diamond II.

The chi square limit is set to be 1e-8, so the problem mentioned in the earlier section can be fixed and the reconstructed pattern will be even more similar to the original diffraction pattern after feedback iteration algorithms. The amount of iterations determines the efficiency of phase retrieval test. The sample is made of 100x100 pixels and the oversampling ratio is 9. In addition, the initial phase is equal to 0. Afterwards, three tests that were performed on the same sample with coherent X-ray, X-ray from Diamond I and Diamond II to form diffraction patterns were conducted respectively.

Firstly, the horizontal emittance of the X-ray beam from I13 beamline is 3.14e-9m/rad and the horizontal emittance will be reduced by a factor of 20 after the upgrade. Sigma x equals 2.509e-6m and 5.611e-7m before and after the upgrade. The vertical emittance of the X-ray in Diamond is 8.81e-12m/rad, so sigma y after the calculation is 1.329e-7m. Considering the vertical or y component of the emittance has no effect due to the upgrade, sigma y will be fixed at 1.329e-7 m. Then, the diagrams of CDC, in figure 33, depicts the intensity of light on the surface of the sample right before penetration. The intensity will be uniform and equal to 1 in the ideal coherent wave case. For Diamond I, the light has slightly higher intensity horizontally distributed in the middle of the sample, whereas the more coherent light from Diamond II has a wider range of uniform intensity in the centre of the sample. As suggested, in figure 33, the shape of CDC in Diamond II is elliptical because sigma x is not equal to sigma y. For Diamond I, the shape of CDC was supposed to be elliptical, but it seems to be horizontal lines due to the huge difference between sigma x and y.

The number of iterations are all the same and equal to 49, no matter if the sample is shined with coherent X-ray, X-ray beams from Diamond I or Diamond II. Rather surprisingly, the chi square diagrams of these tests have the exact pattern in figure 33. Therefore, one can conclude that decreasing the horizontal emittance of the X-ray beam in Diamond I does not improve the quality of the reconstructed diffraction pattern nor the sample. Moreover, both results from Diamond I and Diamond II match with the ones from the ideal coherent wave-front case.

There are three potential reasons for such a phenomenon to occur:

- The chi square limit should be reduced further. How small should the chi square limit be set is always a problem to be discussed through this entire computing model, because this is an issue of computing costs against the accuracy of the results. On the one hand, the number of iterations will be larger with a smaller chi square limit, so that the smaller difference between each case can be finally seen. On the other hand, the amount of time increases exponentially when the value of chi square limit becomes smaller. For instance, the amount of time it takes the code to run when chi square limit is set to be 1e-3 is 10-15 times more than the case when chi square limit equals 1e-8.

- Computer's limit with small numbers. Since the CDC values from Diamond I and Diamond II fluctuates around 1 with the difference in magnitude of 1e-13, it is very likely for computers to round the values up to 1 and treat it as the ideal case. This can explain the same pattern of the chi square against iterations for the three cases.

- Our model does not account for the changes in brilliance between Diamond I and Diamond II. From both research and our field trip to Diamond it was found that the reason for the upgrade in the I13 branch line was more specifically aimed towards the time it takes to perform the experiment rather than coherence of the beam. As our code didn't account for this we were unable to account for its contribution

4.2.3 – Further modelling

In this section, further ability of this computing model is tested. The goal is to retrieve the phase and reconstruct the sample for any pictures or antisymmetric object.
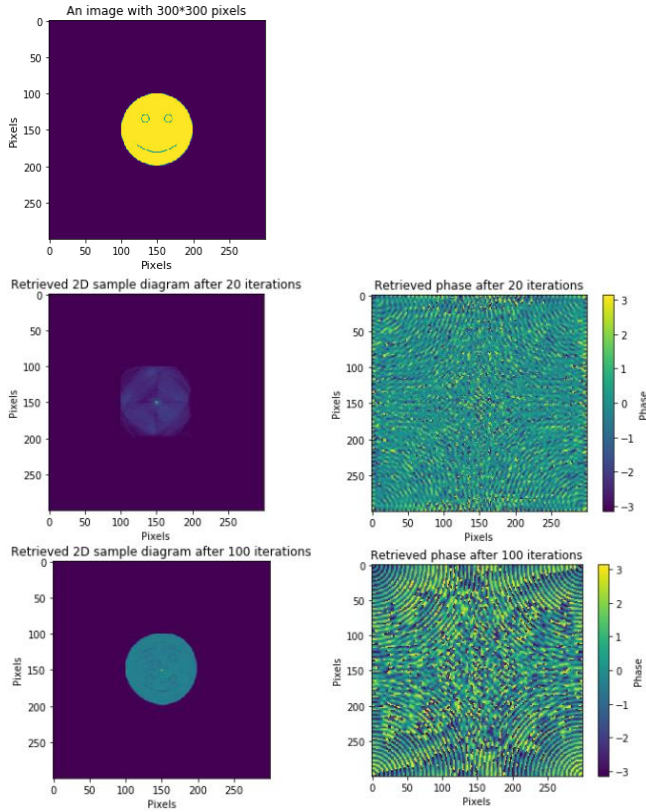
a) ER+HIO algorithms

Figure 34: A group of figures of original sample, retrieved phase and samples after 20 and 100 iterations.

A smiley face image with 100x100 pixels is converted from jpg form to numerical arrays in python. Having set the oversampling ratio to 9, the density of the image was normalized to fit the grayscale which the density varied from 0 to 1. Then, applying the ER and the HIO algorithms to the sample whilst the initial phase of the sample is 0. As seen from figure 34, the sample and the phase are reconstructed after 100 iterations. Despite the circular shape of the reconstructed smiley face matches with the original image, it has two major issues. Firstly, the density of the recovered sample is not the same as the original one, because there is a bright high density point in the middle of the face, this has caused the code to fail in normalization the density pattern. Secondly, the code is facing a symmetry problem. This means the code was designed in a way that only symmetrical objects can be reconstructed. In figure 34, the smiley face after 100 iterations has split into two faces in the opposite direction with respect to the horizontal axis. These are difficult problems to be solved within a limited amount of time. Therefore, a special case of the ER algorithm, the GS algorithm is introduced.

b) GS algorithm

The benefit of the GS algorithm is that the symmetry problem no longer exists. It works by assuming the intensity pattern is homogeneous and has intensity normalized to 1 $v^2(m)^{-\frac{1}{2}}$. Without applying the oversampling criteria, the image can be recovered as follows:
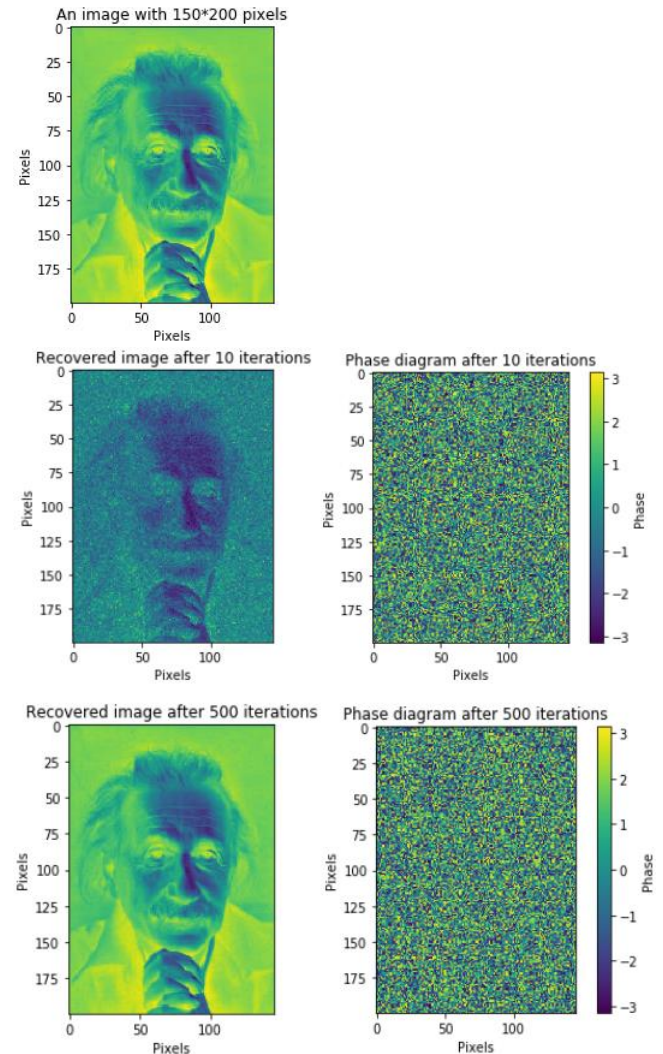

Figure 35: a group of figures of the image of Albert Einstein, retrieved phase and images after 10 and 500 iterations.

The face of Einstein is reconstructed after 500 iterations. The phase diagram seems to be random through these 500 iterations. Thus, the diffraction pattern will never be recovered and this is the biggest drawback of the GS algorithm.

5 - Conclusion

Diamond I's upgrade will require a great deal of changes making use of and developing the latest novel technologies and techniques to ensure it reaches its potential new parameters. The main improvements will be made to the storage ring, increasing the synchrotrons beam energy from 3.0 GeV to 3.5 GeV, and reducing the horizontal emittance by a factor of 20. The experimental capacity of Diamond II will also see improvement - five new beamlines will come into operation in addition to the existing 33 bringing the total number to 38 beamlines. This means that the scientific output of the facility will increase for future generations enabling more cutting-edge research to be developed at the facility to help progress the academic community. Such a large project would also lead to developments in other fields as the upgrade has not only engineering challenges but great operational and logistical challenges that will test the limits of scientific and engineering minds alike in the strive to make Diamond II a reality.

With this stated the need to remain competitive with other worldwide synchrotrons is another factor in the decision to develop the Diamond II upgrade. The Diamond Light Source, as a crucial world-class synchrotron, has been contributing to the research and development of many industrial sectors around the world. The UK can only continue to support such scientific investigations if they can overcome the global competition set out by the numerous upgrade programmes taking place around the world. As discussed in the main body of the report, planned upgrade programmes currently being established at the world's top third-generation synchrotron light sources such as ESRF-EBS, Elettra 2, Petra IV, SLS-2, are another driver in the decision to develop the Diamond II facility. Due to the extreme theoretical growth during the past 20 years in the fields of medicine and material science, the user community is constantly demanding for better and more sophisticated experimental facilities. With the planned Diamond II upgrade, more accessible local high-tech equipment would be available for eagerly demanding European scientists to utilise. Furthermore, with the advancements in the field of telecommunications, there is an increase in the number simultaneous research projects taking place in different facilities across the world. Therefore, if Diamond II is to result in a successful upgrade, it could open a variety of opportunities to contribute to the more advanced and collective global research proceeding at fourth-generation light sources.

From analysis of the computational models for both current Diamond I and Diamond II it was found that the differences in the resolution of the images of the sample before and after the upgrade were negligible. This is because both Diamond I and the planned Diamond II have extremely near coherent beams, due to their low emittance and thus the iteration process for Diamond II will only slightly be improved. Thus, if we drastically increased the precision of our model by for example decreasing the value of the chi-square limit this may have been observed. However, this would have taken up far too much computational time to simulate and so was not possible in our investigation.

This result leads to the conclusion that Diamond II is not a significant upgrade to Diamond I however this does not account for another variable, brilliance. When considering the brilliance of Diamond II's x-rays in comparison to the brilliance of Diamond I's x-rays there is a significant increase in brilliance in Diamond II. The increase in brilliance results in more data being collected per pulse due to the increased number of nearly coherent photons per unit area. This means that experiments post upgrade will be able to construct the images faster due to the larger volume of points in which the algorithmic code would be able to analyse from, leading to a drastic increase the number of experiments that are performed at diamonds I13 branch line. With the increased number of experiments the academic output of the facility would remain world leading, resulting in the facility being not only more accessible to future scientists but also allowing an increased rate of production and advancement in the scientific fields that would benefit from this technique. With that stated, due to the high difficulty in coding a model that accounts for both the brilliance and emittance, this justification for Diamond II was only investigated with theory.

Investigation into the range of research currently operating in Diamond I found that many projects will benefit greatly from the improvements in spatial, dynamic, and energy resolutions. For instance, life scientists will have the chance to explore structures down to atomic scale while still maintaining a large field view (approximately at the scale of millimetres). Apart from structural characterisation, the dynamics of living organisms will also be available for research as the time and duration of each x-ray pulse has been increased to microseconds which due to most biomolecular processes happening at a slower rate then what was previously possible at Diamond I are now possible in Diamond II. For physical scientists, Diamond II will deliver transformative gains in many areas of research in physics, chemistry, materials science and engineering. The increase in brightness and coherence will allow observations to be made at the sub-micron scale, and even nanometre scales, using coherent diffraction techniques or even observations at time resolutions of tens of nanoseconds.

Despite a large amount of public investment being required in order to develop and run such facilities, the socio-economic impacts provide a positive return on investments. In addition to the research and development of various scientific fields, a more indirect effect is appreciated by the economy. First of all, it improves the average quality of life as industries develop more cutting-edge products and more business opportunities are discovered based on the research. Since Diamond I is located in a low populated area, there is

an increase in the economic activities as more unrelated jobs are also created as a result of the facility. Lastly, investment into science and research shapes the future of the upcoming workforce, as they apprehend more skills as a direct result of the scientific discoveries.

From this investigation it is evident that the impact of such an upgrade cannot be understated, especially during a time of technological innovation and immense leaps in the progress of scientific research. It is clear that the upgrade will bring a multitude of benefits in many forms to a range of communities, as well as to the United Kingdom as a whole and globally. Ultimately in the long run, the upgrade will pay for itself and contribute massively to science, and we look forward to seeing the success of Diamond II.

6 - References

[1] P. Willmott, An Introduction to Synchrotron Radiation, UK: Wiley, 2011, pp. 39-67.

[2] "Simulations and Worksheets," Diamond Light Source, [Online]. Available: https://www.diamond.ac.uk/Public/For-School/Resources/Simulations-and-Worksheets.html. [Accessed 16 2 2020].

[3] "Inside the Synchrotron," Canadian Light Source, [Online]. Available: https://www.lightsource.ca/inside_the_synchrotron. [Accessed 16 2 2020].

[4] H. Koivisto, "Particle Sources Part I: Electron Sources," CERN, 4 3 2013. [Online]. Available: https://indico.cern.ch/event/218284/contributions/1520599/attachments/352241/490774/Part_1_-Electron_sources.pdf. [Accessed 16 2 2020].

[5] "Bird's eye view of the synchrotron," Diamond Light Source, 2018. [Online]. Available: https://www.diamond.ac.uk/Science/Machine/Components.html. [Accessed 16 2 2020].

[6] B. Shepherd, "Conventional Magnets for Accelerators," The Cockcroft Institute, 2016. [Online]. Available: https://www.cockcroft.ac.uk/wp-content/uploads/2016/07/magnets_l1.pdf. [Accessed 16 2 2020].

[7] A. Milanese, "An introduction to Magnets for Accelerators," John Adams Institute, 25-26 Jan 2017. [Online]. Available: https://indico.cern.ch/event/590390/contributions/2381025/attachments/1401281/2140074/JAI_course_Jan_2017.pdf. [Accessed 16 2020].

[8] J. Als-Nielsen and D. McMorrow, Elements of Modern X-ray Physics, Chichester, West Sussex: Wiley, 2011, pp. 30-67.

[9] "WHAT IS A BEAMLINE?," ESRF, [Online]. Available: https://www.esrf.eu/about/synchrotron-science/beamline. [Accessed 17 2 2020].

[10] "SIXS," Soleil Synchroton,[Online], Avaliable: https://www.synchrotron-soleil.fr/en/beamlines/sixs.[Accessed 26/03/2020].

[11] "Diamond-II", Diamond Light Source, [Online]. Available: https://www.diamond.ac.uk/Home/About/Vision/Diamond-II.html. [Accessed 25/03/2020]

[12] L. A. M. A. C. Abraham, "Diamond-II: Conceptual Design Report," Diamond Light Source, Didcot, 2019.

[13] Alekou, A., Bartolini, R., Carmignani, N., Liuzzo, S. M., Raimondi, P., Pulampong, T., & Walker, R. P. (2018). Novel Double Triple Bend Achromat (DTBA) lattice design for a next generation 3 GeV Synchrotron Light Source. arXiv preprint arXiv:1801.02522.

[14] M. Trubetskov, "Multilayer optics for ultrafast applications," 2015 Conference on Lasers and Electro-Optics (CLEO), San Jose, CA, 2015, pp. 1-2.

[15] "Diamond II: Advancing Science" Diamond Light Source, 2018. [Online]. Available: https://www.diamond.ac.uk/dam/jcr:2ddff8c5-80fe-43aa-8a00-321be9c02cc6/Diamond%20II%20Science%20Interactive%20_%20Dec%202019%20Update.pdf. [Accessed 25 3 2020].

[16] G. Terstappen and A. Reggiani, 2001. In silico research in drug discovery. *Trends In Pharmacological Sciences*, 22(1), pp.23–26.

[17] F. Petruzzellis et al., "The pitfalls of in vivo imaging techniques: evidence for cellular damage caused by synchrotron X-ray computed micro-tomography", *New Phytologist*, vol. 220, no. 1, pp. 104-110, 2018. Available: 10.1111/nph.15368.

[18] A. Bar-Even et al., "The Moderately Efficient Enzyme: Evolutionary and Physicochemical Trends Shaping Enzyme Parameters", *Biochemistry*, vol. 50, no. 21, pp. 4402-4410, 2011. Available: 10.1021/bi2002289.

[19] [3]A. Bar-Even et al., "The Moderately Efficient Enzyme: Evolutionary and Physicochemical Trends Shaping Enzyme Parameters", *Biochemistry*, vol. 50, no. 21, pp. 4402-4410, 2011.

Available: 10.1021/bi2002289.

[20] W.R. Nitske, "The life of Wilhelm Conrad Röntgen", discoverer of the X ray / by W. Robert Nitske, Tucson: University of Arizona Press, 1971.

[21] C. Detlefs, "An Upgrade for the European Synchrotron Radiation Facility", Snchrotron Radiation News, 21(1), pp.35–40, 2008.

[22] T. Bouvet, C. Detlefs, E. Mitchell, and JL. Revol, (2007). "The ESRF Science and Technology Programme 2008–2017", Grenoble, France: ESRF. Available at: http://www.esrf.eu/Apache_files/Upgrade/ESRF-SciTechProg2008-2017.pdf [Accessed 10 Feb. 2019]

[23] G. Admans, and A. Joly, (2018). "ESRF Highlights 2017". Grenoble, France: ESRF. Available at: https://www.esrf.eu/Apache_files/Highlights/HL2017.pdf [Accessed 10 Feb. 2019]

[24] https://photon-science.desy.de, (2012). DESY. [online] Available at: http://hasylab.desy.de/news__events/announcements/coherent_x_ray_scanning_microscopy_at_petra_iii_reached_10_nm_resolution_june_2012/index_eng.html

[25] A. Bharti, N. Goyal, "Fundamental of synchrotron radiation". Department of Physics, Panjab University, Chandigarh, India: IntechOpen, 2019.

[26] P. Raimondi, "ESRF-EBS: The Extremely Brilliant Source Project". Synchrotron Radiation News, 29(6), pp.8–15. 2016.

[27] ESRF-EBS. "EBS Storage Ring Technical Report". ESRF Design Report, 2018.

[28] P. Thompson, et al., "New opportunities for the XMaS beamline arising from the ESRF upgrade program". AIP Conference Proceedings, 2054(1), pp.Proceedings Of The 13th International Conference On Synchrotron Radiation Instrumentation, 2019.

[29] N. Martensson, & M. Eriksson, "The saga of MAX IV, the first multi-bend achromat synchrotron light source". Nuclear Inst. and Methods in Physics Research, A, 907, pp.97–104, 2018.

[30] MAX IV, (2010). "MAX IV Detailed Design Report. Technical Report". Lund, Sweden.[online] Available at: https://www.maxiv.lu.se/accelerators-beamlines/accelerators/accelerator-documentation/max-iv-ddr/

[31] Daniel G. Smith," Huygens' and Huygens–Fresnel Principles"2013

[32] Miao, J., Charalambous, C., Kirz, J. & Sayre, D. (1999*a*) *Nature (London)*, 400, 342–344.
.

[33] R. W. Gerchberg and W. O. Saxton, "A practical algorithm for the determination of the phase from image and diffraction plane pictures," Optik 35, 237 (1972)

[34] J. R. Fienup, ''Phase retrieval algorithms: a comparison,'' Appl. Opt. 21, 2758–2769 (1982)

[35] J. R. Fienup and C. C. Wackerman, "Phase-retrieval stagnation problems and solutions," J. Opt. Soc. Am. A 3, 1897-1907 (1986)

[36] Heinz H. Bauschke, Patrick L. Combettes, D. Russell Luke, "Hybrid projection–reflection method for phase retrieval", Vol. 20, No. 6/June 2003/J. Opt. Soc. Am. A

[37] R. W. Gerchberg and W. O. Saxton, "A practical algorithm for the determination of the phase from image and diffraction plane pictures," Optik 35, 237 (1972)

UCL

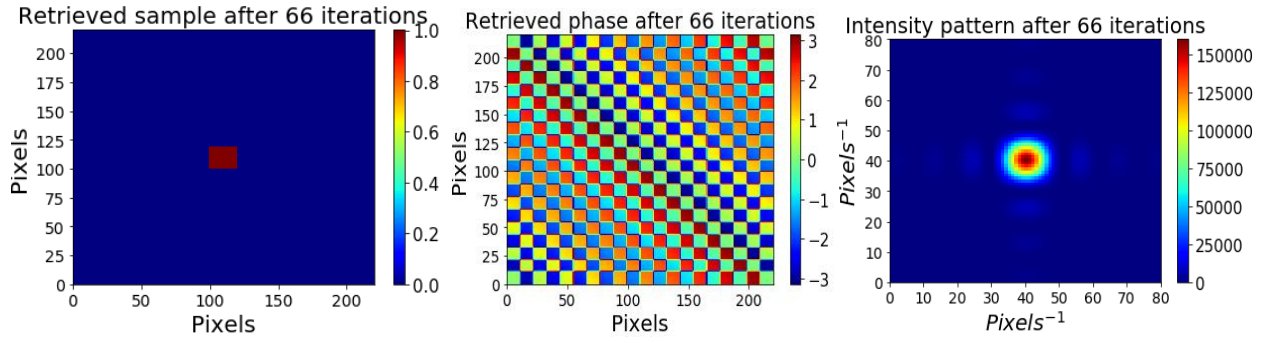# 7-APPENDICES

7.1. Simulated Diagrams
7.1.1
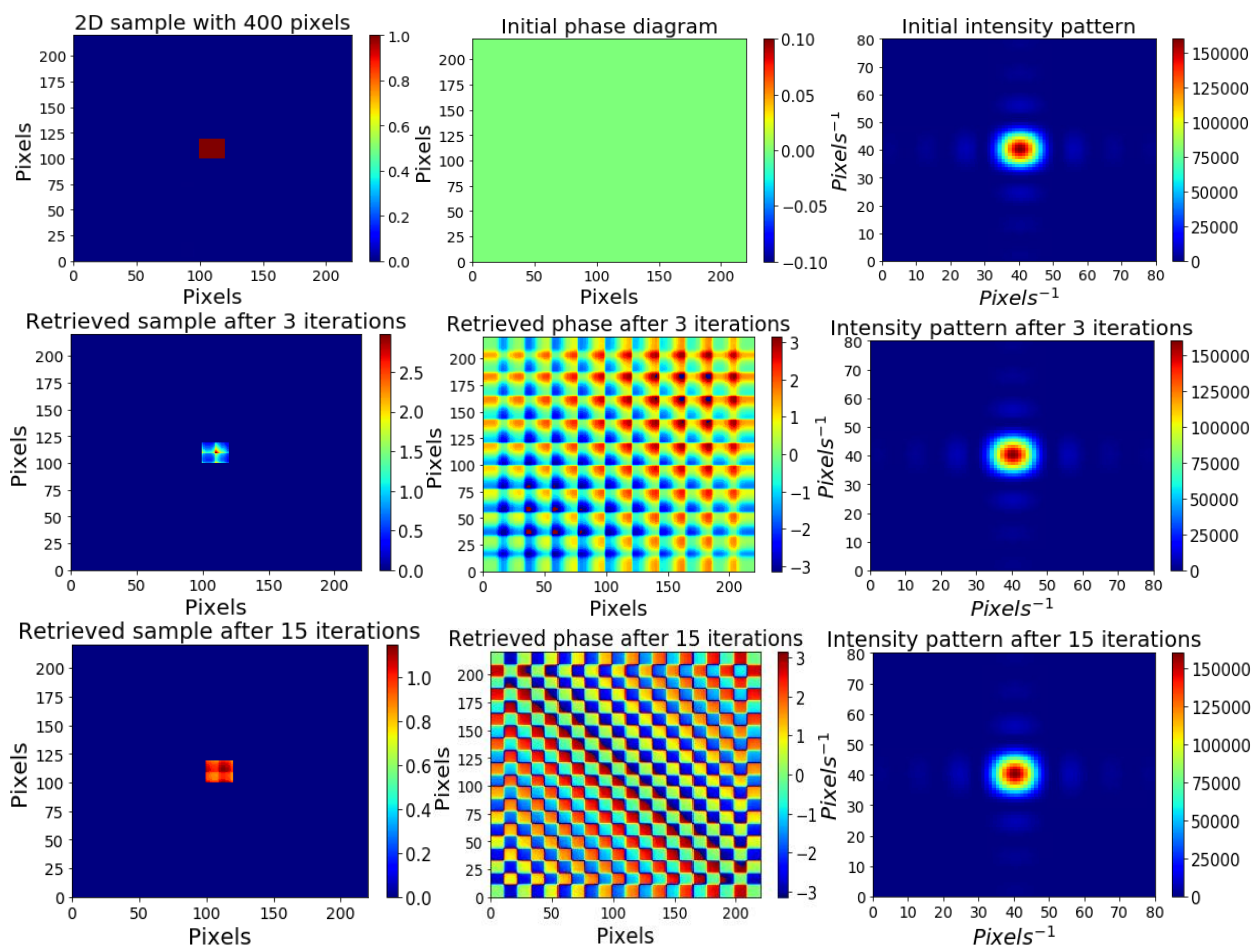
Figure 36: The first row of diagrams shows the original sample, initial phase=0 diagram and the initial intensity pattern. The initial phase diagram is random in this case. The second and the third rows show the recovered sample, retrieved phase and the reconstructed intensity pattern at the 9th and 15th iterations. The last row shows the final results after 66 iterations. The sample is a square with 100*100 pixels and the oversampling ratio is 121.

The chi square of the sample and diffraction pattern (phase=0)
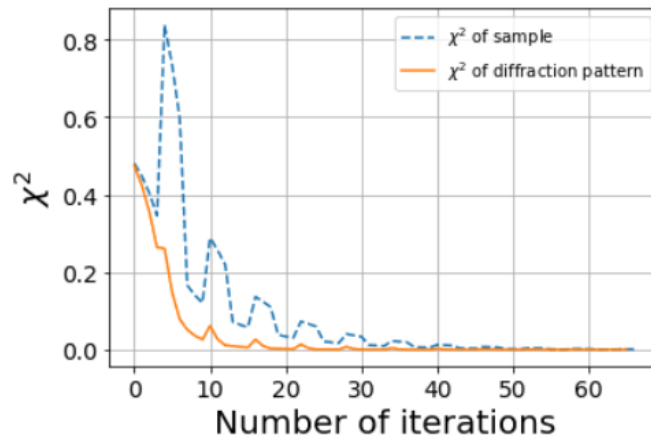
Figure 37: The chi-squared of the sample and diffraction pattern against iterations when the initial phase is equal to 0. The sampling ratio is 121.

7.1.2
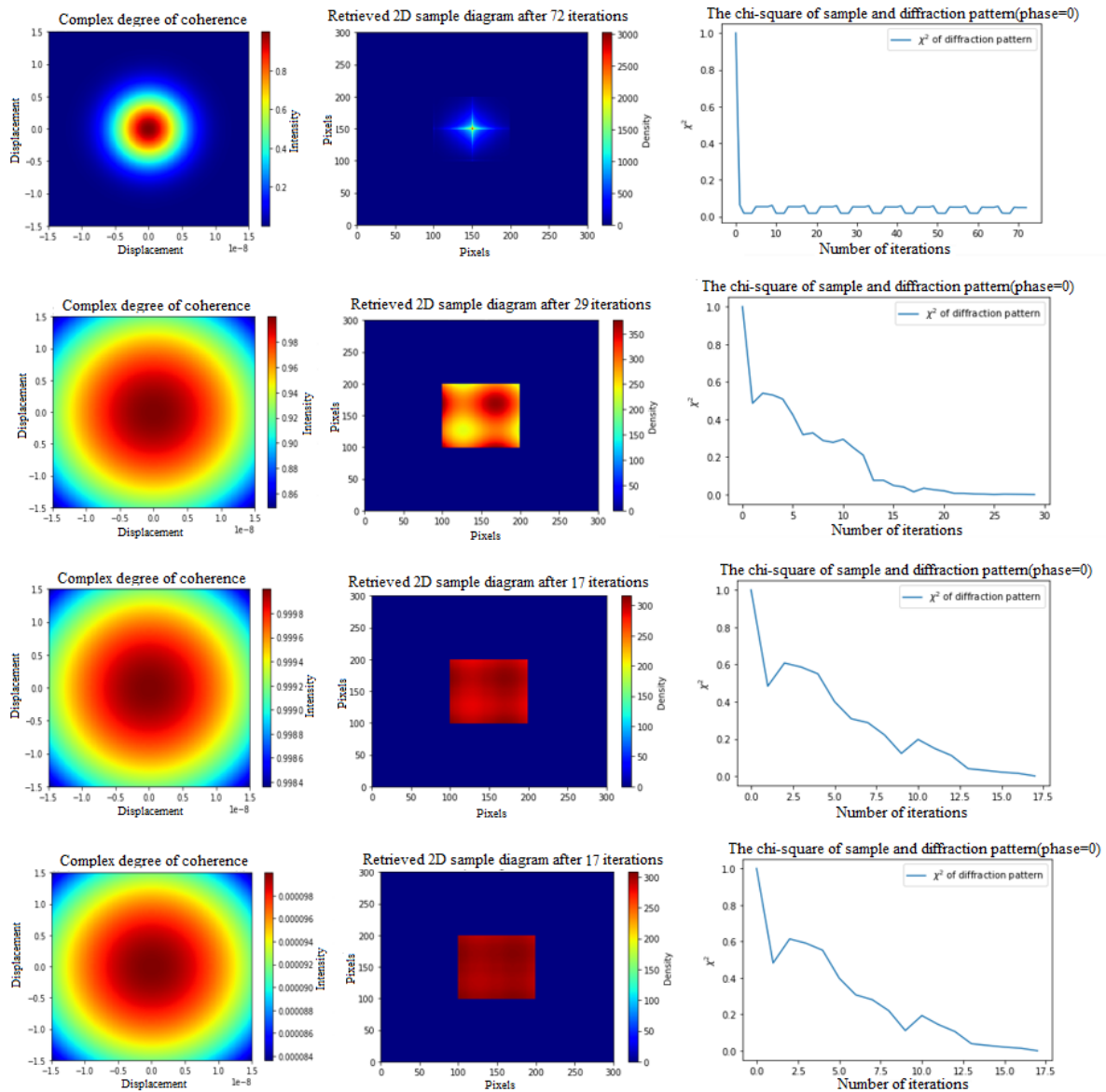
Figure 38: The x and y components of the sigma are equal and each row of the figures have varied sigma values which are equals to 1m, 1e-1m, 1e-2m and 1e-3m respectively. The first column is the complex degree of coherence of the X-ray; the second column shows the reconstructed sample images after retrieving their diffraction pattern to the chi square limit of 1e-3; the last column is the chi square of the sample and diffraction pattern against the number of iterations when the initial phase is 0.

7.1.3
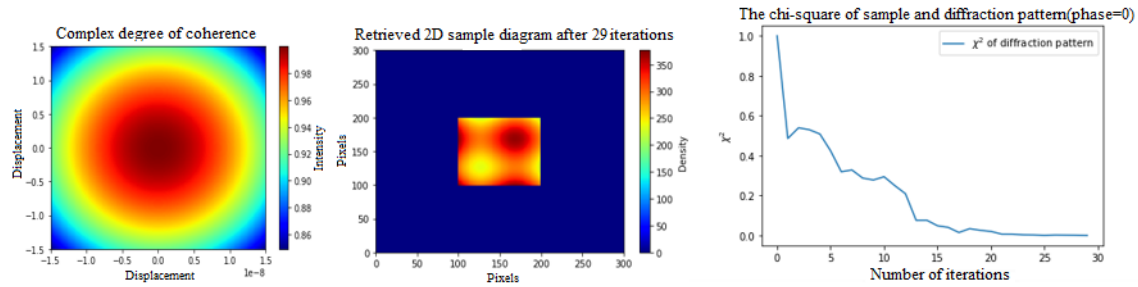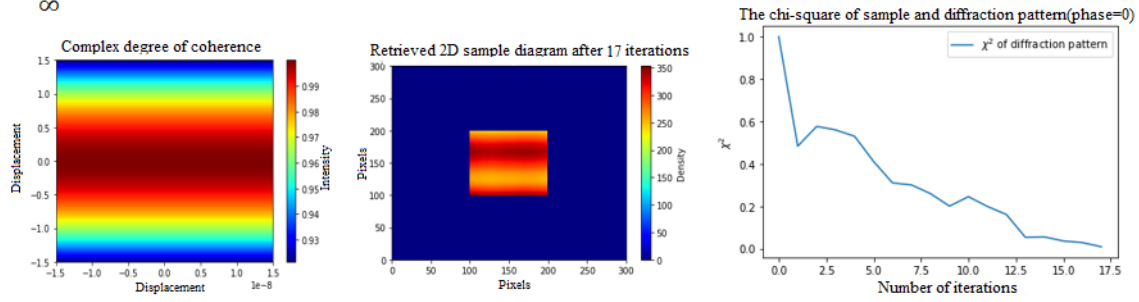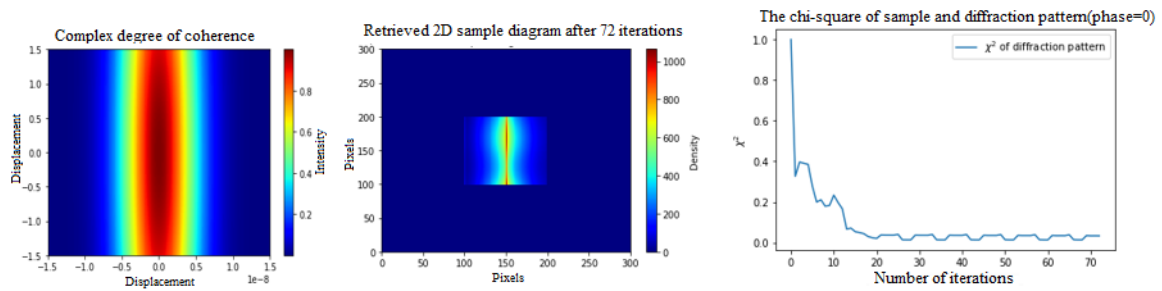
Figure 39: The x component of the sigma is 1e-1m, each row of the figures have the y component of the sigma value equal to 1e-1m, 1/∞m and 1m respectively. The first column is the complex degree of coherence of the X-ray; the second column shows the reconstructed sample images after retrieving their diffraction pattern to the chi square limit of 1e-3; the last column is the chi square of the sample and diffraction pattern against the number of iterations when the initial phase is 0.

8 – Acknowledgments